

Investigation of polarized Synchrotron frequency dependence for CMB observations

A thesis submitted to
Indian Institute of Science Education and Research Pune
in partial fulfillment of the requirements for the
BS-MS Dual Degree Programme

by

Raagini Abhay Patki



Indian Institute of Science Education and Research Pune
Dr. Homi Bhabha Road,
Pashan, Pune 411008, INDIA.

April, 2020

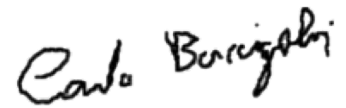
Supervisor: Prof. Carlo Baccigalupi
Co-supervisor: Prof. Tarun Souradeep


© Raagini Abhay Patki 2020


All rights reserved

Certificate

This is to certify that this dissertation entitled **Investigation of polarized Synchrotron frequency dependence for CMB observations**, towards the partial fulfilment of the BS-MS dual degree programme at the Indian Institute of Science Education and Research (IISER), Pune represents study/work carried out by Raagini Abhay Patki at Scuola Internazionale Superiore di Studi Avanzati (SISSA) under the supervision of Prof. Carlo Baccigalupi, Astrophysics and Cosmology Group, and at IISER Pune under the co-supervision of Prof. Tarun Souradeep, during the academic year 2019-2020.


Prof. Carlo Baccigalupi


Prof. Tarun Souradeep

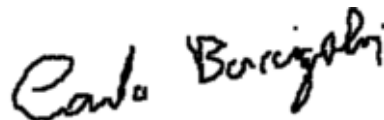

Raagini Abhay Patki

Committee:

Prof. Carlo Baccigalupi

Prof. Tarun Souradeep

Prof. Prasad Subramanian



This thesis is dedicated to my grandmother, Pramila Wamanrao Deshpande.

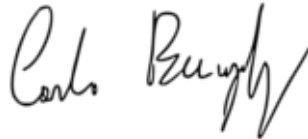
Declaration

I hereby declare that the matter embodied in the report entitled **Investigation of polarized Synchrotron frequency dependence for CMB observations**, is the result of the work carried out by me at Scuola Internazionale Superiore di Studi Avanzati (SISSA) under the supervision of Prof. Carlo Baccigalupi, Astrophysics and Cosmology Group, and at IISER, Pune under the co-supervision of Prof. Tarun Souradeep, and the same has not been submitted elsewhere for any other degree.



Raagini Abhay Patki

Prof. Carlo Baccigalupi



Prof. Tarun Souradeep



Acknowledgment

I sincerely thank Prof. Carlo Baccigalupi for his continuous guidance and support, right from choosing the topic of this thesis to its present completion. I am also thankful to him for helping me gain exposure to the broader aspects of this field through various opportunities. I would like to express my deepest gratitude to Dr Nicoletta Krachmalnicoff for persistently guiding me closely throughout this project. It would not have been possible without her constant support, motivation and expertise.

I am extremely grateful to Prof. Tarun Souradeep for his continued encouragement and advice throughout the past two years, and for many helpful discussions and suggestions. I also thank Prof. Prasad Subramanian for supporting and evaluating this thesis as a member of my thesis advisory committee. Special thanks to Dr Davide Poletti for his valuable inputs and useful discussions.

Finally, I would like to thank my parents, sister and brother-in-law for their unfailing support and encouragement. A big thank you goes to all my friends at SISSA and IISER, and to good coffee, for making this whole journey even more enjoyable and fun!

Abstract

Hunting for the faint B-mode polarization of the Cosmic Microwave Background (CMB) is an open problem today, since it would provide direct evidence for primordial gravitational waves. Moreover, the CMB B-mode would be a powerful probe of inflationary models, and the fundamental physics driving them at energy scales way beyond the reach of particle accelerators. Characterization and removal of contaminating foregrounds that dominate over this primordial signal is a crucial observational challenge. We investigate the diffuse Galactic synchrotron emission, which is the dominant contaminant at frequencies below 70-100 GHz. We reconstruct its synchrotron spectral index (β) map on 30% of the sky, by modelling polarization as a Rician random variable, due to noise in the measurements. We combine low-frequency WMAP and Planck polarization datasets with radio data from S-PASS, in a Bayesian framework.

We first test our method on simulations and find that it recovers unbiased estimates of the true spectral index, by using MCMC to estimate errors on β . Combining fewer datasets gives less accurate estimates, motivating the inclusion of additional datasets for improved constraints in the future, using our method. Applying to our real data, we recover a mean $\beta = -3.21 \pm 0.12$. We introduce a threshold that identifies around 75% pixels with reliable estimates of β . We show that spatial variation of synchrotron polarization is a real feature beyond noise effects, and find it to be higher than reported earlier. We also calculate the power spectrum of the β map to quantify its scale dependence. More realistic simulations can be built using our results, which are crucial for testing component separation. This work can also be extended to forecast the impact of spatial variation of synchrotron polarization on its level of contamination and foreground removal, which are extremely relevant for upcoming CMB experiments.

Contents

Abstract	vii
1 The cosmic microwave background	1
1.1 Big Bang cosmology	1
1.2 Cosmic inflation	2
1.3 Recombination and origin of the CMB	4
1.4 CMB Polarization	6
1.5 Statistics and power spectra	8
1.6 Status of observations	10
2 CMB foregrounds	15
2.1 Major contaminants	15
2.2 Contamination to B-modes	19
2.3 Parameterization of Synchrotron and recent studies	20
3 Methodology and Datasets	23
3.1 Modeling synchrotron polarization	23
3.2 Datasets	25
3.3 Method of reconstructing the synchrotron spectral index	27

4	Validation on Simulations	31
4.1	Generating simulated datasets with PySM	31
4.2	Estimating the spectral index deterministically	32
4.3	Estimating the spectral index using MCMC	36
5	Results on Data	43
5.1	Reconstructed spectral index map with errors	43
5.2	Identifying reliable pixels	46
5.3	Angular power spectrum	48
5.4	Discussion	49
6	Conclusions and Outlook	53

Chapter 1

The cosmic microwave background

The cosmic microwave background (CMB) is the oldest electromagnetic radiation in the Universe. It was emitted from the surface of last scattering (SLS) about 380,000 years after the Big Bang. The CMB encodes critical information about the Universe in its energy spectrum, variations in intensity and polarization across the sky. While most of the signal in intensity fluctuations has been measured accurately, most recently by the Planck mission, only about 10% of the polarization signal in the CMB sky has been extracted. Today, the removal of diffuse Galactic foregrounds is the main limiting factor in extracting the CMB polarization signal from observations.

In this chapter, we introduce the standard Big Bang model of cosmology, relevant theory of the CMB and the current status of its observations. We then move on to foreground emissions and our specific problem in the subsequent chapters.

1.1 Big Bang cosmology

Einstein's theory of General Relativity provided a concrete framework for the Standard Model of cosmology, which assumes that the Universe is spatially homogeneous and isotropic at large scales; a fair approximation according to most observations. Spacetime is then described by the Friedmann–Lemaître–Robertson–Walker (FLRW) metric,

$$ds^2 = dt^2 - a^2(t) \left(\frac{dr^2}{1 - kr^2} + r^2(d\theta^2 + \sin(\theta)^2 d\phi^2) \right), \quad (1.1)$$

where $a(t)$ is the scale factor and k is the curvature.

In 1929, based on measurements of their redshifts, Hubble [1] discovered that distant galaxies appear to be receding away at a velocity proportional to their distance to us. Today, we have ample and robust evidence from several astronomical *standard candles* that the Universe is expanding. The Big Bang model describes how the Universe expanded from a state of hot and dense plasma to subsequently evolve into the large-scale structure (LSS) in the distribution of galaxies (i.e. tracers of matter) in the Universe today. The success of this model is mainly due to the observational confirmation of its predictions of the Hubble expansion, light element abundances explained by 'Big-Bang nucleosynthesis' (BBN), and the CMB radiation.

The expansion is quantified by the Hubble parameter, $H(t) \equiv \frac{da/dt}{a}$, which measures how rapidly the scale factor increases with time. Einstein's field equations relate the evolution of $H(t)$ to the energy content in the Universe, leading to the Friedmann equations, one of which is given below:

$$H^2(t) = \frac{8\pi G}{3} \left[\rho(t) + \frac{\rho_{cr} - \rho_0}{a^2(t)} \right], \quad (1.2)$$

where $\rho(t)$ is the total energy density as a function of time with ρ_0 as the value today, and $\rho_{cr} \equiv \frac{3H_0^2}{8\pi G}$ is the critical density.

In an expanding Universe, the physical distance between two points is proportional to the scale factor times their spatial co-ordinate differences or *comoving distance*, which remains fixed. The maximum comoving distance travelled by light since the beginning of time is defined by the particle horizon χ_P ,

$$\chi_P(a) = \int_0^t c \frac{dt}{(a(t))} = \int_0^a \frac{c}{aH} \frac{da}{a}. \quad (1.3)$$

Two regions could have been causally connected only if their separation is less than the particle horizon size. The Hubble radius, $\chi_H(t) \equiv \frac{c}{aH}$ sets the size of the observable Universe; it is the characteristic distance scale at which all dynamical processes get damped due to cosmological expansion.

1.2 Cosmic inflation

While the Standard Model is successful in predicting the overall evolution of a smooth, homogeneous Universe, it is inadequate for understanding the LSS of galaxies and the anisotropies in

the CMB. Perturbations around a smooth FLRW Universe need to be considered for this purpose, which evolve according to the Einstein-Boltzmann equations and eventually give rise to the observed structures [2]. A fundamental question that remains then, is: how did these perturbations originate in the early Universe? The most plausible explanation for the generation of these initial conditions is the theory of inflation.

Inflation was originally introduced [3][4] as a solution to some major problems of the Big Bang model of cosmology, including the horizon problem. The Universe is quite isotropic at large scales - the CMB temperature map observed (Figure 1.1) is isotropic to one part in 10^5 . Now, equation (1.2) predicts that the Hubble radius only increases with time, so the largest length scales should have come into causal contact only recently. Then, how could the photons at the SLS share the same temperature, while being separated by a distance of many particle horizons?

The basic idea of inflation is that there was an epoch of accelerating expansion just after the Big Bang, during which vacuum energy dominated the Universe, and the scale factor grew by around 60 e-folds in $10^{-34}s$. Consequently, widely-separated regions in the CMB were microscopically close and in causal contact before inflation, which allowed them to be in thermal equilibrium. Post-inflation, this would lead to the isotropic temperature background that we observe today. Inflation also solves other major problems of the Big Bang model, namely the flatness problem, and the absence of unwanted relics and of magnetic monopoles from the breakdown of symmetry of the postulated fundamental unified force [5].

Typically, inflation is driven by a generic scalar field ϕ in a potential V , which sources the vacuum energy. Quantum mechanical fluctuations occurring in ϕ produce scalar, vector and tensor perturbations in the metric, that are Gaussian. Scalar perturbations couple to density fields, and thus provide the initial seeds for structure formation after inflation. Tensor perturbations are characterised by two components h_+ and h_\times , and are also known as gravitational waves.

There are a plethora of proposed models of inflation today. However, it lacks direct observational evidence, since in most models, the energy scales involved are of order 10^{15} GeV, which are way beyond the reach of particle accelerators. The detection of primordial gravitational waves would be a solid evidence in support of the theory of inflation. The most promising window for this detection is by observing their unique signature in the CMB polarization (Section 1.4), which could not only constrain inflationary models, but also probe the fundamental physics driving them.

1.3 Recombination and origin of the CMB

1.3.1 A perfect blackbody

A few seconds after the Big Bang, the Universe became very homogeneous and isotropic at large scales, as a consequence of inflation. The Big Bang model predicts that light nuclei were formed within the first three minutes. Current estimates of light element abundances are consistent with those from Big Bang Nucleosynthesis (BBN), further confirming this model [6].

The few months old smooth Universe consisted of a hot plasma of dark matter, electrons, baryons, neutrinos, and photons. To successfully reproduce the light element abundances through BBN, the number density of photons in this plasma is expected to be much larger than that of baryons, given by their ratio $\eta = \frac{n_\gamma}{n_b} \approx 10^9$, (which remains almost constant across time) [7]. This fact has been spectacularly reconfirmed by precise measurements of CMB intensity fluctuations [8]. The high density and temperature induced frequent collisions that maintained thermal equilibrium in the baryon-photon plasma, and also kept it ionised; any formed atom would get ionised instantly by the high-energy photons.

As the Universe expands, the wavelength of photons gets stretched, and their energy decreases. At one point, the mean photon energy in the early Universe dropped below the binding energy of hydrogen (~ 13.6 eV), but due to the large η , there were still enough energetic photons in the tail of the distribution to keep it ionised. As the Universe continued to expand, there were fewer energetic photons to ionise the bound electrons, and the photon mean free path λ_γ increased. The Saha equation predicts that when the temperature dropped to $\sim 3000K$ (at $z \approx 1100$), the electrons combined with nuclei to form the first neutral atoms, termed 'Recombination'.

Since the photons could no longer scatter and ionise the atoms, the λ_γ grew and reached the Hubble radius. The photons decoupled from matter and started free streaming from the SLS, while the Universe became transparent for the first time. Since the plasma was in thermal equilibrium before this phase transition, the released photons followed a blackbody spectrum. Cosmological expansion maintained this distribution, while lowering its characteristic temperature to about 2.73 K at present. This radiation is observed as the CMB today. The COBE (Cosmic Background Explorer) satellite's intensity measurements in 1994 [9] confirmed that the CMB is indeed a near-perfect blackbody.

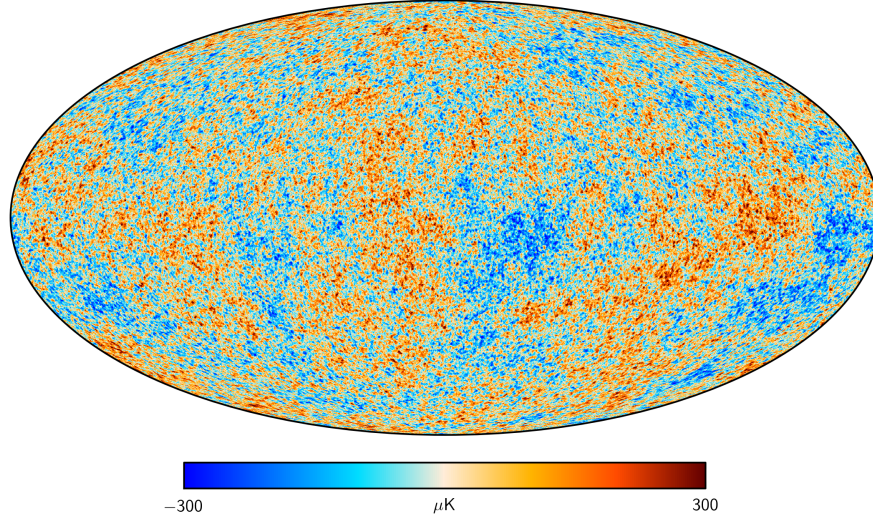


Figure 1.1: Temperature anisotropies in the CMB observed by Planck, map obtained from SMICA [10]

1.3.2 CMB temperature anisotropies

While the CMB is quite isotropic, deviations from the mean temperature of ~ 2.73 K have been observed at the order of $\Theta \equiv \frac{\Delta T}{T} \approx 10^{-5}$ (Figure 1.1). These temperature anisotropies in the CMB are a projection of the photon perturbations at recombination on the SLS. While they are quantitatively explained well within Big Bang cosmology (Section 1.5), their origin can also be understood qualitatively.

Inflation had seeded small perturbations in the density fields. Thus, matter fell into gravitational wells of slightly overdense regions. While the dark matter component did not interact with the photons, it was gravitationally coupled to baryons. As baryonic matter got compressed, radiation pressure increased against the gravitational pull. This mechanism set up gravito-acoustic oscillations in the baryon-photon plasma, which accounts for much of the temperature anisotropies at recombination [2].

In order to compare the temperature anisotropy field of the CMB in observations with theory, it is useful to separate this field at different length scales. This is done by expanding it in terms of spherical harmonics, which form a complete basis for scalar fields over a spherical surface:

$$\Theta(\hat{n}) = \sum_{lm} a_{lm} Y_{lm}(\hat{n}). \quad (1.4)$$

1.4 CMB Polarization

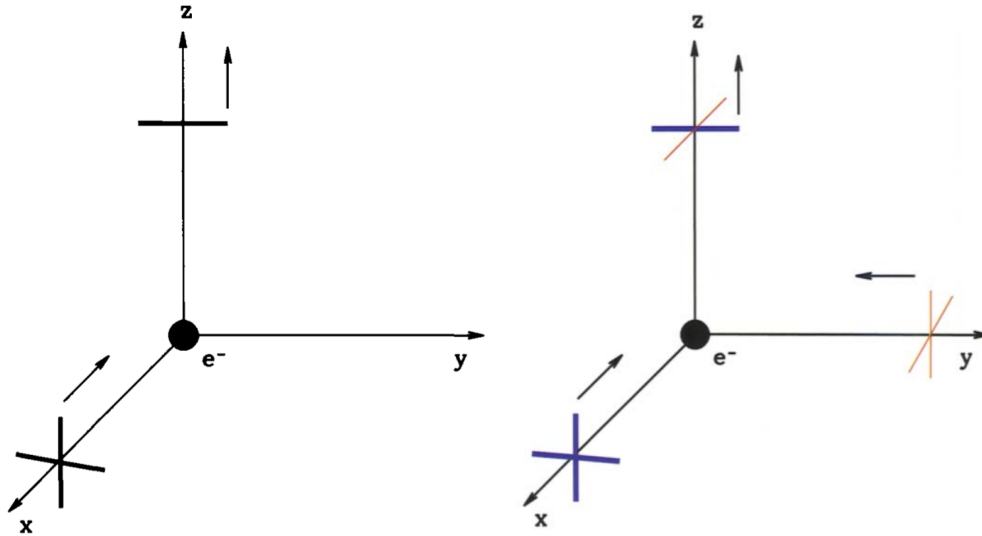


Figure 1.2: A single unpolarized incident ray gets polarized after Compton scattering (left). Compton scattering of quadrupole radiation result in linearly polarized light (right). Figures reprinted from Modern Cosmology, Dodelson [10]

The temperature fluctuations field only encodes part of the information that the CMB holds; the radiation is also polarized. As shown in Figure 1.2, Compton scattering only allows transverse radiation to pass, while blocking the component parallel to the outgoing direction. Considering radiation from all directions, it can be shown that only the quadrupole moment of the incident field (the $l = 2$ mode in equation (1.4)) can produce polarized light after Compton scattering.

The CMB radiation is characterised by the 2×2 intensity tensor I_{ij} in a 2D coordinate basis of measurement:

$$I_{ij} = \begin{pmatrix} I+Q & U \\ U & I-Q \end{pmatrix} \quad (1.5)$$

Here I , Q and U are the Stokes parameters ($V=0$ since Compton scattering does not produce circular polarisation). I is the temperature field, while Q and U locally define the polarisation. The disadvantage of this representation is that it depends on the coordinate system. The E/B harmonic decomposition was proposed as a more useful and physically relevant description [11]. In analogy with equation 1.4, the linear polarisation field can be expanded in terms of spin-2

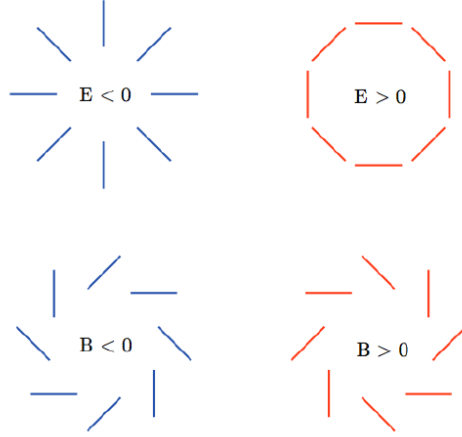


Figure 1.3: E- and B-mode polarisation patterns. Reprinted from Baumann et al.(2009) [12]

spherical harmonics;

$$(Q \pm iU)(\hat{n}) = \sum_{lm} \pm 2a_{lm} \pm 2Y_{lm}(\hat{n}). \quad (1.6)$$

The E- and B- components are then defined as:

$$a_{lm}^E = -\frac{1}{2}(+2a_{lm} + -2a_{lm}), \quad (1.7)$$

$$a_{lm}^B = \frac{i}{2}(+2a_{lm} - -2a_{lm}). \quad (1.8)$$

The E- and B-modes of polarisation have distinct geometrical behaviour. The direction of greatest change in the polarization is parallel/perpendicular to the polarization for E and at 45° to the polarization for B. Based on this property, we can intuitively understand a crucial result - scalar perturbations cannot generate B-mode polarization [2][13].

A scalar plane-wave perturbation has only one direction associated with it, that of its wavevector \hat{k} . Hence, the photon distribution from it is rotationally symmetric about \hat{k} . Now the polarization produced from this perturbation only knows one direction \hat{k} , which dictates both its orientation and the direction of changing strength, giving a pure E-mode. On the other hand, tensor perturbations having a shear component can induce an azimuthal dependence on the photon distribution, and can therefore generate both the E- and B-modes. If vector perturbations are produced during inflation, they decay away, and are negligible during recombination [13]. Therefore, measuring the CMB B-mode will be a direct evidence of non-scalar cosmological perturbations, and in particular primordial gravitational waves.

1.5 Statistics and power spectra

While cosmological models do not predict the exact temperature map in Figure 1.1, they do make statistical predictions about the anisotropies. Inflation generates tiny Gaussian perturbations, which act as the initial seeds for structures in the Universe. Due to the radiation pressure of photons, the density perturbations in the baryon-photon plasma remain small and 'linear' before recombination. Thus, we expect the CMB anisotropies to be highly Gaussian (with a mean of zero), as seen in current measurements.

The distribution of CMB anisotropies is then completely characterized by their variance. Since it is useful to separate scales in harmonic space (equations (1.4), (1.7), (1.8)), the relevant statistic is defined as the angular power spectrum C_l

$$\langle a_{lm} a_{l'm'}^* \rangle = C_l \delta_{ll'} \delta_{mm'}. \quad (1.9)$$

The CMB is described by four angular power spectra: those for T, E, B and the cross correlation between T and E. Cross correlations between B and T or B and E vanish since they have opposite parities. Assuming statistical isotropy, each C_l can be estimated from the $(2l+1)$ independent a_{lm} values;

$$C_l^{XY} = \frac{1}{2l+1} \sum_{l=-m}^m (a_{lm}^{*X} a_{lm}^Y); \quad (1.10)$$

where $XY = TT, EE, BB, TE$. Since there are a finite number of spherical harmonics at any given l , there is a fundamental limit on the uncertainty of C_l , called cosmic variance: $\left(\frac{\Delta C_l}{C_l}\right) = \sqrt{\frac{2}{2l+1}}$.

Models predict the angular power spectra C_l^{XY} , which can be obtained numerically by solving Boltzmann equations using codes such as CAMB (Code for Anisotropies in the Microwave Background) [14]. Figure 1.4 shows measured TT and EE CMB power spectra by past CMB experiments, with best-fit predictions to the data from Planck [8]. These C_l 's carry a wealth of cosmological information; some broad features are discussed here [7]. Acoustic oscillations in the primordial plasma leave a series of peaks in the TT spectrum. It peaks at a $l \sim 180$ (corresponding to an angular scale of 1°), which matches with the Horizon size at the SLS, as predicted theoretically. The CMB power spectra are sensitive to the composition of the energy content of the Universe. For example, an increase in the baryon content enhances compressions of the plasma due to extra gravity, which leads to an increased disparity between the heights of odd and even numbered peaks, known as baryon loading [2]. Cosmological photons have a non-zero mean free

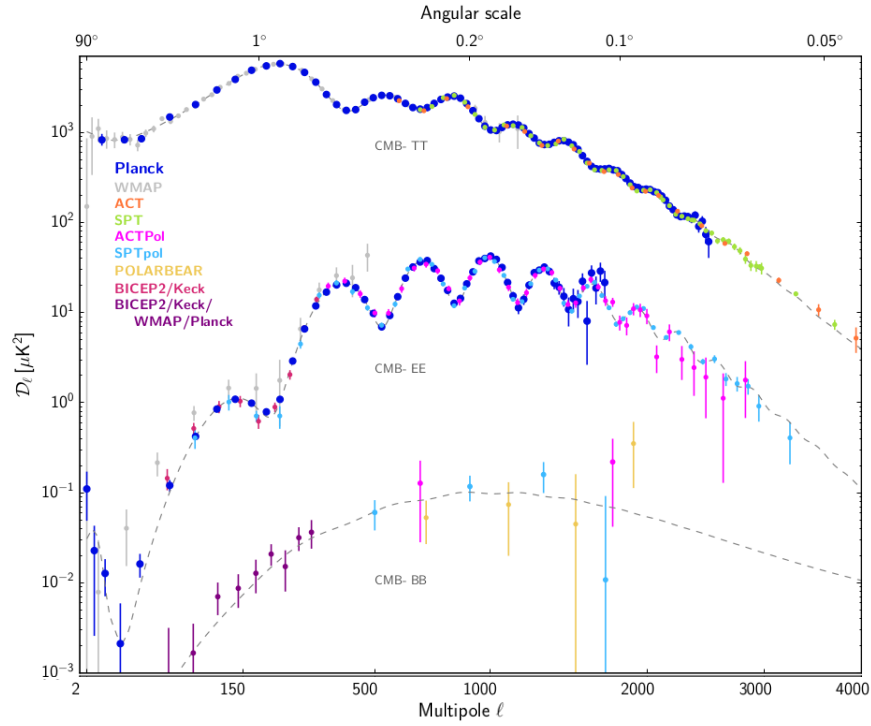


Figure 1.4: Recent measurements of CMB angular power spectra for TT, EE and lensed-BB. Different experiments are shown with different colours, each retaining its original binning. The dashed line shows the best-fit Λ CDM to Planck temperature, polarization and lensing measurements. Reprinted from Planck Collaboration (2018) [8]

path between scatterings with the tightly coupled electrons. So, for scales smaller than the mean distance travelled by photons in a *Hubble time*, the perturbations get washed out. This process is known as Silk damping [15], and leads to a progressive exponential damping of the spectrum at larger l s (or smaller scales). The TT spectrum at low l s, and its overall tilt are determined by the properties of cosmic inflation. The acoustic peaks in the EE power spectrum occur when velocities peak, and are thus out of phase with the TT peaks. Since polarisation is sourced by the temperature quadrupole anisotropies, which are quite small, the amplitude of C_l^{EE} is much smaller than that of C_l^{TT} . The BB power spectrum C_l^{BB} is discussed in the following Section and Section 2.2.

1.6 Status of observations

Following the discovery of the CMB in 1964 by Penzias and Wilson [16], the COBE satellite confirmed the blackbody spectrum of the CMB and statistically detected temperature anisotropies. Launched in 2001, the WMAP (Wilkinson Microwave Anisotropy Probe) satellite measured the CMB TT, TE and EE power spectra using 5 frequency channels, for angular scales of $l = 2$ to 1000. [17]. For a full list of current and upcoming CMB experiments, refer to the LAMBDA website hosted by NASA [18].

1.6.1 Measurements from Planck

The successor to WMAP was the satellite Planck, which was operated by the ESA (European Space Agency) from 2009 to 2013. Planck mapped the sky in 9 frequency channels, with a much higher sensitivity, and measured the CMB TT, TE and EE power spectra accurately. Figure 1.4 shows the detected CMB TT and EE power spectra from Planck and other ground-based telescopes like ACT (Atacama Cosmology Telescope) and SPT (South Pole Telescope).

The Λ -CDM (Λ -Cold Dark Matter) is a parameterization of the Big Bang model, and is now regarded as the 'Standard model of cosmology'. With six free parameters, defined briefly in Table 1.1, it is the simplest model that agrees well with most of the cosmological observations. By fitting for the CMB and lensing power spectra, the Planck collaboration has found good consistency with the baseline Λ -CDM model, and has provided the tightest constraints on its parameter values at percent level accuracy [19]. While these results agree well with BAO and Supernovae data, there

Parameter	Best-fit values	Description
$\Omega_b h^2$	0.02233 ± 0.00015	Baryon density today
$\Omega_c h^2$	0.1198 ± 0.0012	Cold dark matter density today
$100\theta_{MC}$	1.04089 ± 0.00031	Approximate acoustic angular scale at the SLS
τ	0.0540 ± 0.0074	Reionization Optical depth
$\ln(10^{10} A_s)$	3.043 ± 0.014	Primordial curvature power spectrum amplitude
n_s	0.9652 ± 0.0042	Spectral index of primordial scalar perturbations

Table 1.1: Baseline Λ -CDM best-fit parameter constraints, from full combined likelihood analysis of Planck TT,TE,EE + lowE + lensing.[19]

is a 3.6σ tension between the derived value of the ‘global’ Hubble constant today (H_0) provided by Planck, and its direct determination in the ‘relatively local’ neighbourhood.

1.6.2 Current Constraints on B-modes

Unlike the CMB temperature and E-mode polarization, the detection of primordial CMB B-modes is an open observational challenge in cosmology today. This is because the BB spectrum measured by experiments has additional contributions from other sources that dominate over the primordial signal.

In General Relativity, the path of a photon coming from a distant source gets distorted by the presence of matter (or energy), which curves spacetime. This phenomenon is known as gravitational lensing. The distortion of CMB photons due to lensing by the intervening LSS converts some of the the CMB E-modes to B-modes at angular scales below few arcminutes. The POLARBEAR telescope directly measured these lensed B-modes at small scales ($500 < l < 2100$), as shown in Figure 1.4 along with other experiments [20].

As shown in Figure 2.2, the primordial BB power spectrum has a recombination bump at the degree angular scale, which is the acoustic horizon size at the SLS. Like the other CMB power spectra, it is expected to have a series of acoustic peaks which damp further at smaller angular scales. Now, as seen in Section 1.4, while primordial CMB B-modes cannot be generated by scalar perturbations, they can arise due to tensor perturbations. A useful quantity defined in this context is the tensor-to-scalar ratio, r ; it is the ratio of power in primordial tensor perturbations to the power in primordial scalar perturbations. The amplitude of the primordial BB power spectrum thus decreases with decreasing values of r .

There is no theoretical lower limit on the value of r . The tightest observational constraints on r today are < 0.10 from Planck data alone (using TT,TE,EE+lowE+lensing), and < 0.06 from Planck data combined with BAO and BICEP2 data. The primordial B-mode signal is thus expected to be very faint. Again, from Figure 2.2, note that the primordial BB spectrum for $r = 0.10$ is estimated to be smaller than the lensed-BB spectrum at all angular scales. Additionally, at large scales of $l < 20$, the BB signal is boosted further by scatterings that occurred during the epoch of reionization (at redshifts of around 6 to 10). Reionization is primarily characterized by the optical depth of Thomson scattering, best estimated today by measurements from Planck [19].

As we shall see in Section 2.2, the primordial B-modes are also contaminated significantly by diffuse foreground emissions from our own Galaxy. An erroneously large value of r of about 0.2 was reported by [21] from BICEP2 B-mode polarization data. Subsequent analysis revealed that incorrect foreground modelling, especially of thermal dust, was responsible for this error, since the BICEP2 data was largely dominated by Galactic foregrounds [22] [23].

1.6.3 Future Measurements

Ongoing and future CMB experiments aim to detect the primordial B-mode polarization, while estimating the possible value of r . Upper limits on r effectively constrain viable inflationary models, although there is some degeneracy with other parameters (such as n_s) [19]. Since the value of r is directly related to the tensor spectral index and the energy scale of inflation [2][5], by extension, these experiments will also probe the fundamental physics driving inflation.

As mentioned earlier, the POLARBEAR-1 [20] ground-based telescope detected the lensed CMB B-modes at large l in a small fraction of the sky. Its extension, the Simons Array [24], is an ongoing CMB experiment partly consisting of POLARBEAR-2, aiming to detect the lensed and primordial CMB B-modes at small scales. The ACT [25] and SPT [26] have further measured the lensed CMB polarization at very small angular scales. Following BICEP1 and BICEP2, the Keck Array and BICEP3 [27] are telescopes operating from the South Pole, with the goal of constraining the primordial B-modes at their expected peak of degree angular scales. Below, we discuss some of the relevant upcoming experiments which are designed for making more accurate detections.

Simons Observatory (SO) [28]: the SO is a series of ground telescopes being deployed in Chile, operating in 6 frequency channels from 27 GHz-280 GHz. It consists of three 0.4m SATs

that will scan 10% of the sky at degree scales, and one LAT that will scan 40% of the sky at arcmin resolution. SO will aim to detect primordial B-modes at an uncertainty of < 0.003 for an $r = 0$ model, and $r \geq 0.01$ at a 3σ level.

CMB-S4 [29]: CMB-S4 is a planned fourth-generation ground-based experiment, consisting of 500,000 detectors with a net resolution of 3 arcmin. It will be able to achieve an uncertainty of $r < 0.002$ at a 95% CL. CMB-S4 also aims to provide tighter limits on the neutrino mass scale and the number of neutrinos, and test beyond Λ -CDM physics and relics.

LiteBIRD [30]: LiteBIRD is a space-based satellite mission by JAXA with participation of ESA and NASA, and is expected to be launched in 2027. Its main goal is to detect primordial CMB B-modes with an unprecedented accuracy, and a total uncertainty of < 0.001 (for $r = 0$) at a 5σ level. It will be observing in 15 frequency bands across 34–448 GHz. Due to its full-sky coverage, it will access the lowest multipoles, which are crucial for confirming inflation at degree-scales. Thus, it will be complementary to the data from ground-based experiments, while also aiding foreground cleaning and delensing.

Chapter 2

CMB foregrounds

The redshifted spectral energy density (SED) of the CMB corresponds to a blackbody at a temperature of about 2.73 K, with a peak frequency of around 160 GHz. There are many sources of radiation between the SLS and our detectors on the Earth, which emit in this radio-microwave frequency range. In this Chapter, we first introduce the major foreground components contaminating the CMB. We describe their contamination of the CMB B-mode polarization in Section 2.2, and then focus on the specific context of our problem of investigating diffuse Galactic synchrotron emission.

2.1 Major contaminants

On large angular scales, diffuse emissions from our Galaxy are the dominant contaminating foregrounds to CMB observations. Figure 2.1 shows the frequency spectra/Spectral Energy Distributions (SEDs) of foreground components and the CMB, which describe the frequency dependence of the energy of these emissions. The relative contributions are different for temperature/intensity (Stokes parameter I) and for total polarization $P = \sqrt{Q^2 + U^2}$. Note that unlike the CMB, Galactic emissions are non-isotropic, so their strength varies across the sky. Thus, analysis of data is often restricted to masked regions covering a fraction of the whole sky (f_{sky}), by neglecting regions with high contamination. In Figure 2.1, the SEDs of foregrounds are shown as bands, since the level of their emissions varies as masks with different f_{sky} are considered. Here, we describe the physical mechanisms governing each of these foreground components.

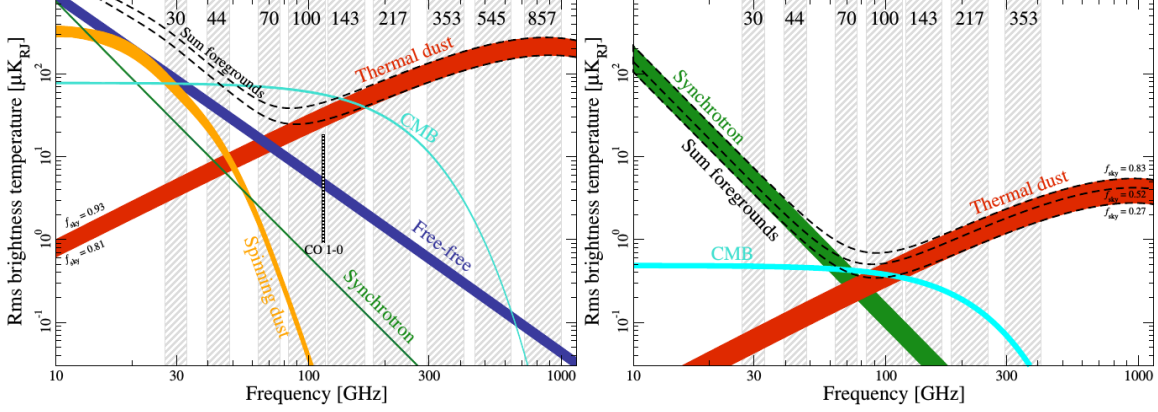


Figure 2.1: Frequency spectra of the CMB and diffuse foregrounds for intensity or temperature (left), and total polarization $P = \sqrt{Q^2 + U^2}$ (right). Widths of the bands for each component show the range for the masks used. Grey bands show the Planck observation channels. Figure reprinted from the Planck 2018 collaboration [8]

2.1.1 Diffuse galactic synchrotron emission

As seen from Figure 2.1, diffuse Galactic synchrotron emission is the dominant contaminant in polarization for frequencies below 70-100 GHz [31] [32]. It is produced by relativistic cosmic ray particles (such as electrons) spiralling in the Galactic magnetic field.

The Galactic synchrotron emission SED is expected to follow a power law across ~ 4 orders of magnitude in frequency [33] as verified in simulations by codes such as GALPROP¹ [34]. This power-law behaviour at intermediate frequencies is well explained physically (see, for example, [35]). First, consider a single relativistic electron (with a Lorentz factor γ) accelerated in a magnetic field B . While it typically emits pulses at its gyration frequency, a fourier transform gives a broad frequency spectrum $E(\nu)$, characterized by a critical frequency

$$\nu_{cr} \simeq \gamma^2 \nu_{cyc}, \quad (2.1)$$

where ν_{cyc} is its cyclotron frequency. The mean power emitted by this electron as observed from an inertial frame is:

$$-\frac{dE}{dt} = (constant) B^2 E^2. \quad (2.2)$$

Now, a population of electrons in a cloud typically have a power law energy distribution $N(E) \propto$

¹<https://galprop.stanford.edu/>

E^{-p} . The specific brightness of synchrotron emission radiated by such a population of particles is given by

$$S(\nu)d\nu = -\frac{dE}{dt}N(E)dE. \quad (2.3)$$

Based on the knowledge of $N(E)$, dE/dt and $dE/d\nu$, the intensity spectrum in antenna temperature units ² is derived to be

$$I_\nu \propto B^{p+1}\nu^\beta, \quad (2.4)$$

with $\beta \approx -\frac{p+3}{2}$. Similarly, the synchrotron polarization frequency spectrum is also expected to follow a power law across a wide range of intermediate frequencies. Beyond this range, the spectrum turns over and cuts off at lower frequencies due to self-absorption. At high frequencies, the spectrum cuts off due to ageing of the source cloud of electrons. From equations 2.1 and 2.2, high-frequencies correspond to highly energetic electrons, which radiate energy away faster. This drop in the number of highly energetic electrons leads to the exponential cut-off at high frequencies. While the basic power law model for the SED describes the higher Galactic latitudes well, it has some limitations close to the Galactic plane, which will be discussed in Chapter 3.

The WMAP Q and U maps at 23 GHz are smoothed to 3° resolution, and are currently used as baseline templates for synchrotron polarization in the PySM (Python Sky Model) software [36]. Fitting these template models and datasets in harmonic space has indicated that the synchrotron power spectrum C_l roughly follows a power law behaviour as a function of multipole l , with an index of $\gamma \simeq -2.6$ [37], with more power at larger angular scales. The index γ is dependent on the Galactic latitude, getting smaller close to the polar caps.

2.1.2 Thermal dust emission

Thermal dust emission is the dominant foreground component above frequencies of about 100 GHz, in both intensity and polarization. The interstellar medium in our Galaxy has dust consisting of polycyclic aromatic hydrocarbons (PAHs), carbonaceous and silicate grains. The grains are heated to temperatures of around 10-30 K by absorption at optical frequencies, and are cooled by emission in the far-infrared [38]. Aspherical dust grains tend to align perpendicular to the magnetic fields, and preferentially emit along their longest axis, resulting in polarization.

²Antenna temperature is the temperature of an equivalent perfect resistor that would result in the same power spectral density from an antenna, as the astronomical source. It is related to the unit brightness temperature, defined later in Section 4.1.

The dust SED is well approximated as a modified blackbody with a power-law emissivity coefficient, in the frequency range relevant for CMB observations,

$$I_d = A\nu^{\beta_d}P_\nu(T_d), \quad (2.5)$$

where P_ν is the Planck function for a temperature T_d , and a spectral index of β_d . The Planck data is fitted well by this model with a single temperature T_d of 15.9 K [39], and with slightly different spectral indices for polarization and intensity, owing to multiple components with different polarization properties [36]. The E- and B- mode polarization power spectra for dust are well-fitted by a power law behaviour in l , given by $C_l^{EE} \propto l^{2.42 \pm 0.02}$ and $C_l^{BB} \propto l^{2.54 \pm 0.02}$ for the LR71 sky region covering 71% of the sky, derived from Planck data [8]. The template models for polarized dust maps in PySM are based on the Planck 353 GHz data.

2.1.3 Free-free emission

Free-free or bremsstrahlung radiation is produced by electrons scattering off ions in the warm interstellar medium. The frequency spectrum is well approximated by the two parameter model proposed by [38], based on the emission measure and electron temperature. Free-free emission is theoretically expected to be unpolarized, since the scattering doesn't depend on the direction. Small effects at the edges of ionized clouds can however cause a polarization upto 10%. While free-free emission is a significant contaminant to the intensity in Planck data, its net all-sky polarization is estimated to be below 1% [40].

2.1.4 Anomalous microwave emission (AME)

AME refers to observed excess microwave emission that is not approximated well by known foreground components. It is spatially correlated with thermal dust, and was detected early as a diffuse component in intensity. The most well developed models for AME emission are due to spinning dust grains. One candidate for the AME was proposed by [41] as electric dipole emission from small spinning dust grains. An alternate model attributes AME to magnetic dipole radiation arising from thermal fluctuations in small dust grains. While AME is not thought to be strongly polarized, the polarization fraction is constrained to be less than 1% by the QUIJOTE (QUI JOint TEnerife) experiment [42].

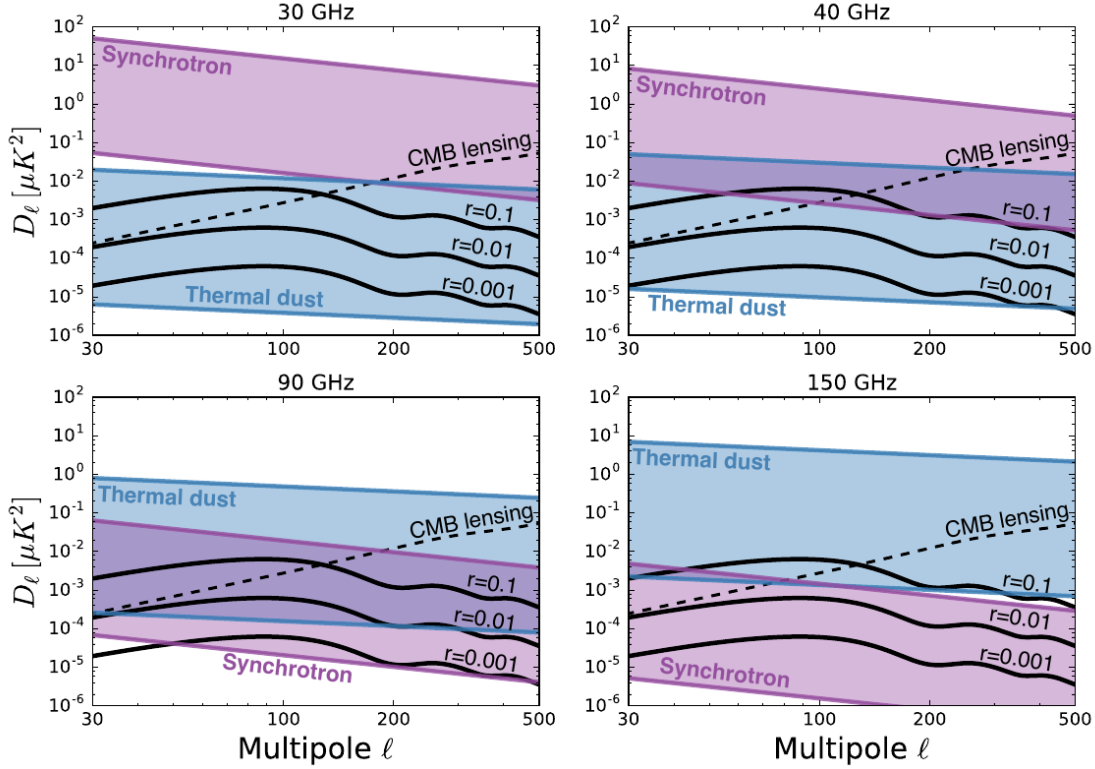


Figure 2.2: Power spectra for primordial CMB B-modes with given values of r and for lensing (according to Planck 2015 Λ CDM best-fit), compared with estimated spectra for synchrotron (violet) and thermal dust, evaluated over 184 regions with $f_{\text{sky}} = 1\%$. Figure reprinted from [37]

Therefore, the major diffuse Galactic foreground components for CMB polarization alone are synchrotron and thermal dust emissions.

2.2 Contamination to B-modes

Upcoming next-generation CMB experiments like LiteBIRD and SO are aiming to detect the primordial CMB B-mode with an accuracy on r of about 10^{-3} . Such a detection would be a robust test of the theory of inflation, and could constrain several inflationary models and their physics. However, the primordial B-mode signal is expected to be very faint; there is no theoretical lower limit on the value of r , and current constraints from Planck T and E-mode data put $r \lesssim 0.10$. Figure 2.2 shows the theoretically predicted power spectra for the primordial CMB B-mode for different values of r , with a peak at degree angular scales. The amplitude for $r = 0.01$ is smaller than that

induced due to lensing by the LSS. Thus, accurate delensing algorithms are required to separate the lensing contribution, especially at smaller \sim arcminute scales. On the other hand, scatterings occurring during reionization in the late-time Universe boost the CMB B-mode at large scales of $l < 20$, which needs to be characterized. In addition to these effects, synchrotron is the dominant polarized foreground component below ~ 70 -100 GHz, while thermal dust emission is dominant at higher frequencies. In Figure 2.2, the spectra for these components are estimated separately on 184 small regions with $f_{sky} = 1\%$. At the level of $r \simeq 10^{-3}$, it is clear that the contamination due to both synchrotron and thermal dust is comparable or greater than the primordial signal, at all relevant frequencies. Thus, removal of foregrounds is the major challenge for detecting the primordial B-mode in observations.

As we prepare for upcoming CMB experiments, there are two broad approaches that address different aspects of this challenge. The first approach is the development of robust data analysis pipelines for separating foreground components from the CMB contribution in observations [43]. These ‘Component Separation’ techniques make use of multi-frequency data and the fact that the spectral shapes of these foreground components and the CMB are all different. The methods of internal linear combination (ILC), template fitting, and independent component analysis estimate the CMB from linear combinations of the maps, while making different assumptions. Parametric model fitting is used to accurately fit sky models for each of the components simultaneously, to give the best-fit parameters through Bayesian analysis. The baseline code COMMANDER used by the Planck collaboration [39] is based on this technique.

2.3 Parameterization of Synchrotron and recent studies

The second broad approach for addressing the challenge of foreground removal in B-mode observations, is to investigate the components themselves in detail, using relevant datasets. Our project belongs to this line of approach, and is focused on characterising the diffuse synchrotron emission as a dominant polarized foreground component at low frequencies.

The Planck maps at 353 GHz and high frequencies are sensitive enough for the characterization of thermal dust polarization and for estimating its level of contamination [39]. On the other hand, the low frequency Planck and WMAP observations go as low as 23 GHz, but do not allow the detection of the synchrotron emission at relevant latitudes. The synchrotron signal is much stronger at lower frequencies; therefore, radio datasets are critical for investigating synchrotron emission

as a contaminant [37]. Combining Planck and WMAP data with data from radio surveys such as S-PASS [44] and C-BASS in the southern hemisphere and QUIJOTE and C-BASS in the northern hemisphere [42] [45] will aid the study of frequency dependence of polarized synchrotron.

The analysis by [37] indicated that at 90 GHz, synchrotron contamination is at the level of an equivalent $r \simeq 10^{-3}$ even in the cleanest regions of the sky. Moreover, there has been evidence of spatial complexity and variation in both thermal dust and synchrotron components [46] [47]. In Figure 2.2, the power spectra of these components appear as wide bands since their degree of contamination varies significantly across the different sky regions. Such studies have important implications about several aspects that need to be considered for building component separation codes and testing their accuracy, and thus crucially complement the first approach described earlier.

The recent work by [37] jointly analysed the angular auto- and cross- power spectra of S-PASS maps with low frequency Planck-30 and WMAP K-band, Ka-band maps, to study the synchrotron foregrounds. More recently, [48] also estimated a synchrotron spectral index map using the S-PASS and WMAP K-band data, by using a simplistic T-T plot technique. In this project, we combine and analyse the same datasets as [37]. However, we do so by instead implementing a mathematically accurate likelihood to model the synchrotron polarization, with the goal of further investigating its spatial behaviour and its frequency dependence. We then forecast how these considerations would impact component separation for CMB experiments in the near future.

Chapter 3

Methodology and Datasets

In this Chapter, we describe the methodology that we have adopted for analyzing multi-frequency datasets of the polarized sky, in order to characterize the diffuse Galactic synchrotron emission as a contaminant in CMB B-mode observations. In Section 3.1, we describe the theoretical model for synchrotron polarization that we fit for using the datasets described in Section 3.2. Finally, we explain our Bayesian approach for estimating the synchrotron spectral index, and derive the relevant likelihood and posterior.

3.1 Modeling synchrotron polarization

Spatial variation and complexity in synchrotron emission is expected due to differences in magnetic field strength and energy distribution of electrons across the sky. So, we must analyze the data maps in real space. Each of the maps are divided into pixels at a specific resolution; to begin with, using a HEALPix [49]¹ grid of $N_{side} = 32$ (about 1.8° sized pixels). At this coarse pixel size, all of our subsequent analysis is done independently for each pixel.

As shown theoretically in Section 2.1.1, the total intensity spectrum of synchrotron emission (corresponding to the Stokes parameter I) has a power-law behaviour in frequency. In our analysis, we only use the Q and U Stokes parameters, and focus on the linear polarization magnitude $P := \sqrt{Q^2 + U^2}$. The polarized intensity spectrum of synchrotron is also expected to follow a power

¹Hierarchical Equal Latitude Pixelization; <http://healpix.sourceforge.net>

law up to first order, across our intended range of frequencies (2.3 to 33 GHz). In each n^{th} pixel, we fit the model SED

$$P_i(n) = A_0(n) \left(\frac{\nu_i}{\nu_0} \right)^{\beta(n)}, \quad (3.1)$$

where $P_i(n)$ is the polarized intensity at a frequency ν_i , $A_0(n)$ is the polarized intensity at a reference frequency ν_0 , and $\beta(n)$ is the spectral index. The frequency dependence is thus controlled by the two free parameters $A_0(n)$ and $\beta(n)$.

While this model is a good approximation at intermediate and high Galactic latitudes, it has certain limitations close to the Galactic plane, for latitudes $|b| \lesssim 20^\circ$. Since the Milky Way is a disc Galaxy, the density of electron clouds and the strength of Galactic magnetic fields are significantly higher at these low latitudes as compared to the rest of the halo. Flattening of the spectrum is more likely to occur close to the Galactic plane due to self-absorption, and due to stacking of multiple synchrotron components along a line of sight.

Discovered by Faraday in 1845, the phenomenon of Faraday rotation refers to the rotation of the plane of polarization of an electromagnetic wave in the presence of a magnetic field. The angle of rotation, θ_r , is related to the magnetic field strength, B_{\parallel} , and the wavelength of the wave, λ , by

$$\theta_r \propto B_{\parallel} \lambda^2. \quad (3.2)$$

While this effect is negligible for WMAP and Planck, it is quite significant at lower frequencies, such as that of S-PASS. At high latitudes, θ_r can reach tens of degrees at 2.3 GHz; however, since the emission is likely to come from a single cloud, the polarization magnitude P that we are using would not get affected much. In contrast, the strong B_{\parallel} close to the Galactic plane can cause a rotation of hundreds of degrees. Differential rotation for multiple clouds sources along a line of sight thus leads to a significant decrease in P at low latitudes, and is called 'Faraday depolarization'.

Therefore, we restrict our analysis to pixels at latitudes $|b| > 20^\circ$, by neglecting regions close to the Galactic plane where these complicating effects are dominant.

3.2 Datasets

We briefly discuss the datasets that we have analysed in this project. As suggested in earlier work [37], radio surveys, such as S-PASS at 2.3 GHz, are crucial for understanding synchrotron emission, due to its high brightness at these low frequencies. We complement the S-PASS maps with the WMAP K-band (23 GHz), WMAP Ka-band (33 GHz) [17], and Planck-30 (28.4 GHz) polarized sky maps [8].

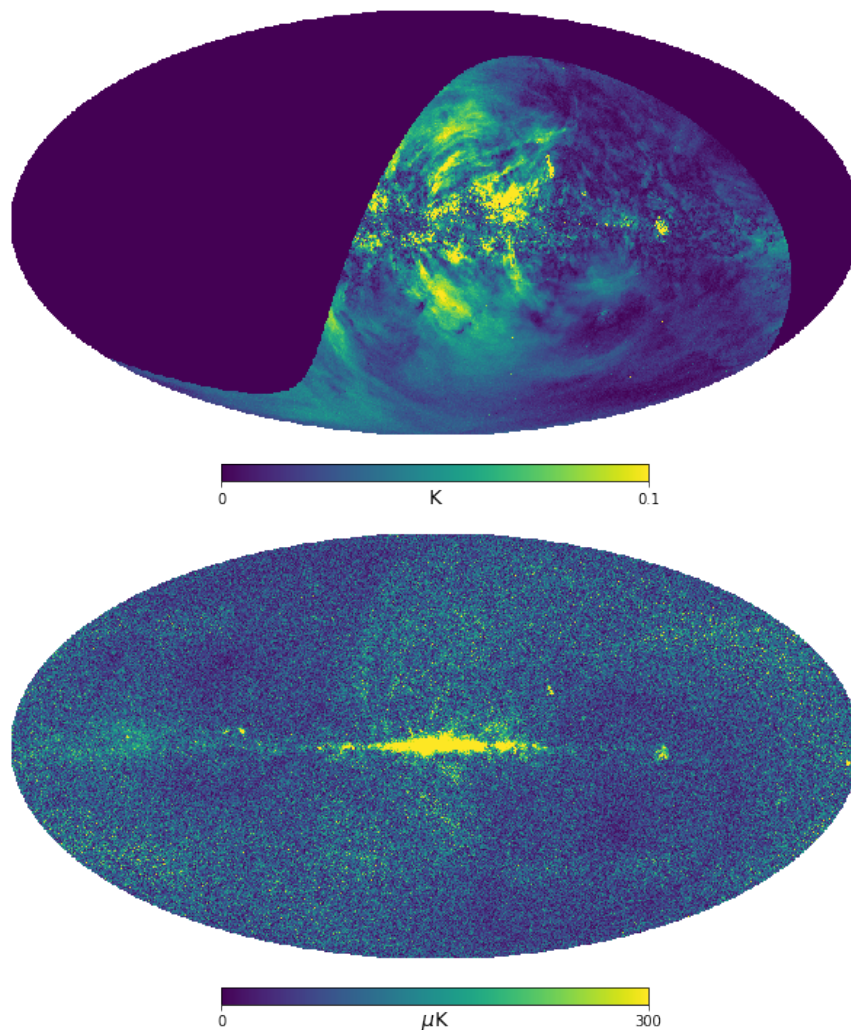


Figure 3.1: S-PASS (2.3 GHz, top) and WMAP K-band (23 GHz, bottom) polarized intensity maps, in brightness temperature units and Galactic coordinates.

We combine the Stokes parameter Q and U maps for each of these datasets to obtain the total polarized intensity ($P = \sqrt{Q^2 + U^2}$). While instrumental white noise is present for each of these datasets, the polarized intensity signal for P drops as a power law with increasing frequencies. As seen in Figure 3.1, the magnitude of P for WMAP K-band (23 GHz) is order of 1000 times smaller than that for S-PASS (2.3 GHz), as expected from a rough spectral index $\beta \approx 3$. So, the signal-to-noise-ratio (SNR) of the S-PASS sky map is much higher than the SNR for the other higher frequency sky maps.

Since the S-PASS data was collected by the ground-based Parkes radio telescope, it covers about half of the sky, specifically the southern hemisphere at $\delta < -1^\circ$. In contrast, the WMAP and Planck data were collected by space-based satellites, and cover the entire sky. Our analysis is thus restricted to the pixels covered by the S-PASS survey. While the S-PASS angular resolution of around $8.9'$ FWHM is much higher than that of WMAP and Planck, we will be downgrading and smoothing all the maps to a common angular resolution.

As seen in Figure 3.1, the WMAP K-band map has a high polarized intensity near the Galactic plane, indicating a strong and structured magnetic field. In comparison, the S-PASS map has virtually no signal at these low latitudes, and shows granularity in the sky map, which is indicative of the Faraday depolarization effect dominant at this low frequency. We will be focusing on the higher latitudes, which are expected to be highly correlated across this 2.3-33 GHz frequency range.

The noise present in the measured Q and U maps for each of the four datasets is characterized as a Gaussian realization of the corresponding noise covariance map. The covariance map at each frequency has been evaluated by the corresponding survey; it describes the spatially varying variance of noise arising due to instrumentation, calibration errors, scanning strategies, etc. Note that since we are not using the I Stokes parameter data, free-free foreground emission is negligible here. Also, the other major polarized contaminant, thermal dust, has a much smaller contribution at these low frequencies; at 23 GHz, its polarized signal strength is about 1% of that of synchrotron, and is almost absent at the S-PASS frequency of 2.3 GHz. Thus, we assume that the Q , U data maps used entirely consist of the polarized synchrotron signal and noise.

3.3 Method of reconstructing the synchrotron spectral index

Assuming the model in equation 3.1, we jointly fit for the two free parameters $A_0(n)$ and $\beta(n)$ independently in each pixel. Our primary goal is to estimate the spectral index $\beta(n)$ map using Bayesian statistics. In this section, we describe the likelihood implemented to model the polarization and the method used.

3.3.1 Polarization as a random variable

Each of the Q and U Stokes parameter maps measured by surveys are a sum of the signal and white Gaussian noise (n_Q, n_U). We make the reasonable assumption that the noise variances are: $\sigma_Q = \sigma_U \equiv \sigma_P$. Consider Q and U as the coordinate axes in a 2D Cartesian plane. Then, measured $P = \sqrt{Q^2 + U^2}$ is the length of the vector in this plane; let ϕ denote the angular polar coordinate. The corresponding coordinates for the true signal are constants, denoted by (P_0, ϕ_0) . Then,

$$Q = P_0 \cos \phi_0 + n_Q; \quad U = P_0 \sin \phi_0 + n_U. \quad (3.3)$$

Since Q and U are independent random variables, the joint probability distribution function (pdf) for (n_Q, n_U) is

$$p_n(n_Q, n_U) = \frac{1}{2\pi\sigma_P^2} \exp\left(-\frac{n_Q^2 + n_U^2}{2\sigma_P^2}\right). \quad (3.4)$$

The expected value of the measured polarization P is then

$$\langle P \rangle_{p_n} = \int_{-\infty}^{\infty} \int_{-\infty}^{\infty} P p_n(n_Q, n_U) dn_Q dn_U. \quad (3.5)$$

Substituting for n_Q and n_U from equation 3.3, and using $dQ = dn_Q$, $dU = dn_U$,

$$\langle P \rangle_{p_n} = \int_{-\infty}^{\infty} \int_{-\infty}^{\infty} \frac{P}{2\pi\sigma_P^2} \exp\left(-\frac{P^2 + P_0^2}{2\sigma_P^2}\right) \exp\left(\frac{QP_0 \cos \phi_0 + UP_0 \sin \phi_0}{\sigma_P^2}\right) dQ dU. \quad (3.6)$$

Transforming to polar coordinates and simplifying,

$$\langle P \rangle = \int_0^\infty P \frac{P}{\sigma_p^2} \exp\left(-\frac{P^2 + P_0^2}{2\sigma_p^2}\right) \left(\frac{1}{2\pi} \int_{-\pi}^\pi \exp\left(\frac{PP_0 \cos \phi_0}{\sigma_p^2} \cos \phi + \frac{PP_0 \sin \phi_0}{\sigma_p^2} \sin \phi\right) d\phi \right) dP. \quad (3.7)$$

The integral in brackets can be simplified by using the standard identity

$$\frac{1}{2\pi} \int_{-\pi}^\pi \exp(a \cos \phi + b \sin \phi) d\phi = I_0(\sqrt{a^2 + b^2}), \quad (3.8)$$

where I_0 is the zeroth order modified Bessel function of the first kind.

$$\langle P \rangle = \int_0^\infty P p(P|P_0, \sigma_p) dP, \quad (3.9)$$

where $p(P|P_0, \sigma_p)$ is the pdf of the polarization P given by

$$p(P|P_0, \sigma_p) = \frac{P}{\sigma_p^2} \exp\left(-\frac{P^2 + P_0^2}{2\sigma_p^2}\right) I_0\left(\frac{PP_0}{\sigma_p^2}\right). \quad (3.10)$$

This is known as the Rician or Rice distribution. Therefore, the measured total polarization P in surveys is a Rician random variable in the presence of noise, for a true signal P_0 .

3.3.2 Bayes Theorem

Bayesian inference from data is a fundamental approach used in modern astrophysics today. It is based on the Bayes theorem in statistics, stated mathematically as follows:

$$p(H|D) = \frac{p(D|H)p(H)}{p(D)}. \quad (3.11)$$

Here, D denotes the data observed by an experiment, while H denotes a hypothesis/theory often parameterized in terms of a theoretical model. Then,

$p(H|D)$: the 'posterior' = the probability that our assumed hypothesis H is true given the observed data D ,

$p(D|H)$: the 'likelihood' = the probability that data D would be observed given the hypothesis H is true,

$p(H)$: the 'prior' = the probability of H being true, prior to the experiment.

$p(D)$ is independent of the considered hypothesis, so it acts as a proportionality constant and can be neglected. We are usually interested in the distribution of the posterior; if we assume a particular theoretical model H to be true, its ‘best-fit’ parameter values will be the ones which maximize the posterior function, given that data D have been observed. This is the essence of the ‘maximum likelihood method’ for parameter estimation that we are following.

3.3.3 Likelihood and Priors

In the context of our problem, we assume the parameterized model given in equation 3.1 (\equiv H) for the true polarized intensity P_0 . The data D in our case is the measured value of P in a particular n^{th} pixel. The likelihood for the n^{th} pixel and a single frequency ν_i is then implied by the equation 3.10:

$$p(P|A_0, \beta, \sigma_P) = \frac{P}{\sigma_P^2} \exp\left(-\frac{P^2 + (A_0(\nu_i/\nu_0)^{-\beta})^2}{2\sigma_P^2}\right) I_0\left(\frac{P A_0(\nu_i/\nu_0)^{-\beta}}{\sigma_P^2}\right). \quad (3.12)$$

i.e. for a pixel n , it is the probability that the value P is measured, given certain values of parameters A_0 and β in our assumed model. In this project, we are considering multiple datasets at different frequencies, each measured independently. The combined likelihood for analysing them simultaneously is then simply a product of the probabilities in equation 3.12 for each used frequency.

We assume an uninformative prior for the parameters. A uniform distribution in the $Q_0 - U_0$ plane corresponds to the prior $p(A_0) \propto (A_0)$. For the spectral index we assign $p((\nu_i/\nu_0)^{-\beta}) \propto \text{constant}$, which gives $p(\beta) \propto |\beta|$. The total posterior distribution is then given by the product of the likelihood and the prior

$$p(A_0, \beta|P_i, \sigma_P) = \prod_i \left(\frac{P_i}{\sigma_P^2} \exp\left(-\frac{P_i^2 + (A_0(\nu_i/\nu_0)^{-\beta})^2}{2\sigma_P^2}\right) I_0\left(\frac{P_i A_0(\nu_i/\nu_0)^{-\beta}}{\sigma_P^2}\right) \right) (A_0|\beta|). \quad (3.13)$$

Thus, in each pixel, we jointly fit for the two free parameters A_0 and β by finding the set of parameter values that maximize this posterior function, given the measured values of polarized intensity P_i at each frequency ν_i . Ultimately, this gives us the estimated spectral index map for the considered frequency range, which largely determines the behaviour of synchrotron emission at other frequencies in different regions of the sky.

Chapter 4

Validation on Simulations

In the previous Chapter, we described our primary methodology for analyzing datasets in order to investigate the diffuse Galactic synchrotron emission. Before applying it to real datasets, we validate it by testing its accuracy and limitations on simulated maps. We first describe the simulated maps and how they are generated in Section 4.1. Then, we implement our methodology using a deterministic technique (Section 4.2) and using MCMC (Section 4.3), and note several observations about the results obtained from the simulated maps.

4.1 Generating simulated datasets with PySM

Throughout this project, we adopted the pixelization scheme given by HEALPix [49] at a resolution of $N_{side} = 32$ ($\sim 1.8^\circ$), and brightness temperature units, for our analysis ¹. I used the Python implementation of HEALPix, *healpy*, as the working environment. We used the PySM (Python Sky Model) [36] software to simulate the Stokes Q and U maps of diffuse Galactic synchrotron emission at the four survey frequencies of our datasets. The WMAP Q and U maps at 23 GHz (K-band) are used as the baseline template in PySM, which were extrapolated to other frequencies by using a simple model of a constant spectral index $\hat{\beta} = -3$ for all pixels. Since Faraday Rotation is negligible at 23 GHz, it can be ignored here, and simulations can be analyzed across the whole

¹In the Rayleigh-Jeans limit (which is valid at the low frequencies that we are considering), brightness temperature is defined as the temperature of an equivalent blackbody that would emit the same intensity/total polarization as the considered source.

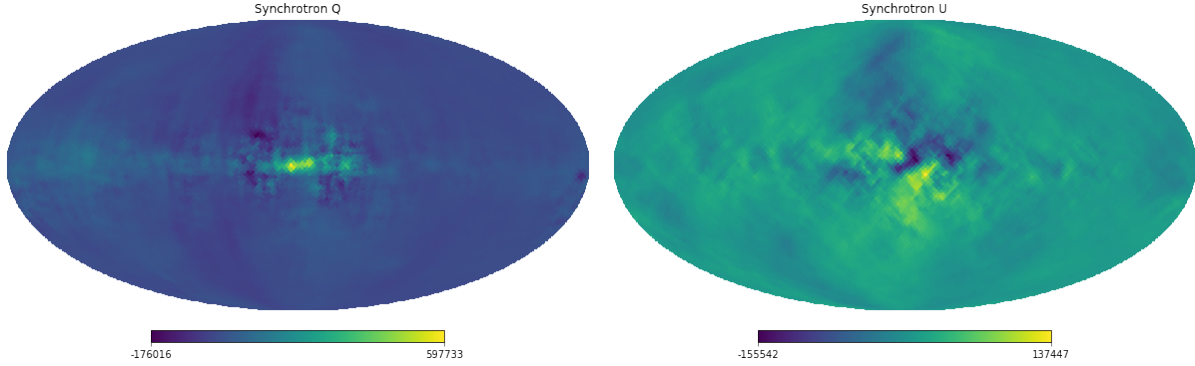


Figure 4.1: Q (left) and U (right) polarization maps of diffuse Galactic synchrotron emission at 2.3 GHz (S-PASS frequency), simulated using PySM [36]. Projection axes for the two Stokes parameter maps are roughly visible. Maps are shown in Galactic coordinates and μK units.

sky. Figure 4.1 shows simulated all-sky maps at the S-PASS frequency of 2.3 GHz.

We added a noise realization to each of these simulated signal maps, and then combined the noisy Q and U maps to get P maps at the four frequencies. For this purpose, we first downgraded the noise covariance maps of the four datasets to an $N_{side} = 32$, using healpy. Figure 4.2 shows the spatially varying noise covariance map for the WMAP K-band dataset at 22.8 GHz. For the pixels not covered by the S-PASS survey, the average noise sensitivity of S-PASS was used as the covariance for 2.3 GHz. Then, in each pixel, a Gaussian noise realization is obtained by multiplying a number drawn from a standard normal distribution by the square-root of the noise covariance for that pixel. The resulting simulated polarization P maps are used as an input for testing our methodology.

4.2 Estimating the spectral index deterministically

As described in the previous chapter, we assume that the diffuse Galactic synchrotron emission follows a power-law SED model (equation 3.1). The geometric mean of the four survey frequencies used is chosen as the reference frequency ν_0 , since it lies well within this frequency range, with a value of ~ 14.89 GHz. We jointly fit for the two parameters A_0 (the polarization amplitude at ν_0) and β (synchrotron spectral index) in each pixel, by finding the parameter values that maximize the posterior function given in equation 3.13. This was initially done deterministically, by using the ‘optimize’ module in scipy and the ‘Nelder-Mead’ optimization algorithm. For the initial guesses,

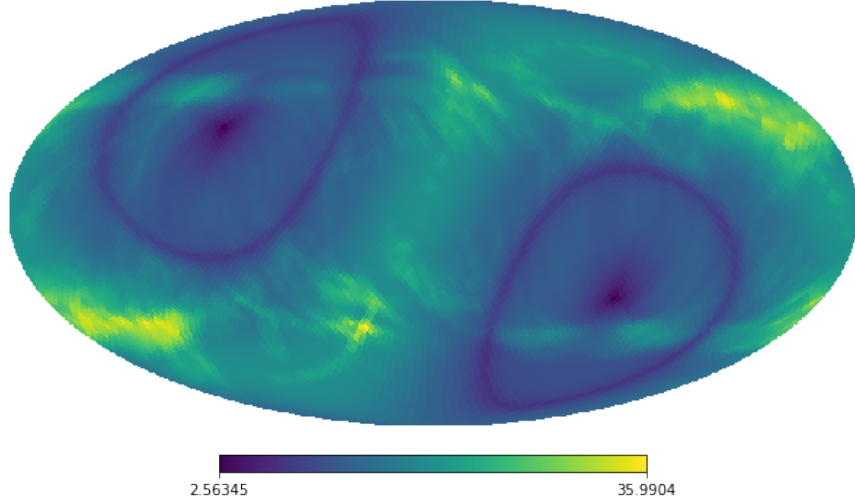


Figure 4.2: Noise covariance map for the WMAP K-band dataset at 22.8 GHz, downgraded to an $N_{side} = 32$. Map is shown in Galactic coordinates and μK units.

the P map simulated at ν_0 with PySM was used for A_0 , while a nominal constant value of -3.6 was used for β . We verified that the algorithm used is fully robust, and the results do not depend on the initial guesses.

We note a technical detail at this point. The posterior function being maximized here contains the likelihood for each frequency as a multiplicative factor; the likelihood, in turn, has a factor of $I_0(PP_0/\sigma_p^2)$ (see equation 3.13). From Bessel function theory, the series expansion for I_0 shows that it increases exponentially as follows

$$I_0(z) \rightarrow \frac{e^z}{\sqrt{2\pi z}} \left(1 + \frac{1}{8z} + \dots \right) \text{ as } z \rightarrow \infty. \quad (4.1)$$

In our case, z is substituted with (PP_0/σ_p^2) which is \approx the square of the SNR. Since the S-PASS P map is nearly noiseless and with very high SNR pixels, the I_0 term for S-PASS is large, and cannot be computed numerically. This issue is solved by computing the logarithm of the function in brackets (I_{0e}) separately, and adding 'z' to it, in order to evaluate the total log-likelihood and posterior. Another implication of this series expansion is the limiting behaviour of $I_0(z)$ at high SNRs (i.e. for $(P_0/\sigma_p) \gtrsim 3$). In this limit, the second and higher terms in the bracket are negligible, so I_0 tends to an exact exponential, and the overall Rician distribution in the likelihood (equation 3.12) quickly approaches a Gaussian distribution. This Gaussian approximation can be used to speed up some of the computations, and also has further implications, which we see in Section

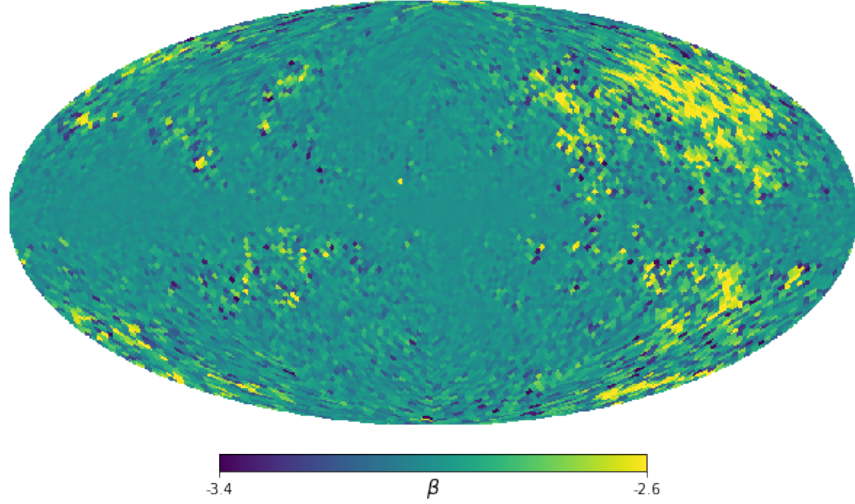


Figure 4.3: Map of spectral index β , estimated from simulated P maps at all the four survey frequencies, with a true value $\hat{\beta} = -3$.

4.3.1.

Our analysis is focused on the estimated best-fit values of the spectral index β , since it largely controls the spectral and spatial behaviour of the synchrotron emission. The map of β shown in Figure 4.3 was estimated using the simulated P maps with a particular random noise realization, at all four frequencies. The average β estimated across pixels is -2.98 ± 0.13 . While this recovered value is in excellent agreement with the true input value of constant $\hat{\beta} = -3$ in our simulations, deviation is observed particularly in some higher-latitude pixels with low SNRs. For each pixel, let S_{min} denote the minimum SNR among the four simulated input P maps. Figure 4.4 shows the scatter between estimated values of β and the corresponding S_{min} for each pixel. Clearly, our method recovers accurate estimates of the true value in most pixels. There is a significant deviation for pixels with very low $S_{min} (< 1)$, indicating that the presence of noise in P maps induces errors on the estimated β values.

The blue histogram in Figure 4.5 shows the distribution of β across pixels in the spectral index map (Figure 4.3), which was estimated by using simulated P maps with one particular set of noise realizations. We repeated the procedure 100 times by taking the same signal maps from PySM and adding 100 different sets of noise realizations to each of them. The estimated 100 β maps were averaged separately in each pixel. The resulting mean β values are plotted as the red histogram in Figure 4.5; the distribution shows that the mean values are close to the true value of -3 used in simulations, for most of the pixels. Thus, we conclude that our method and prior give unbiased

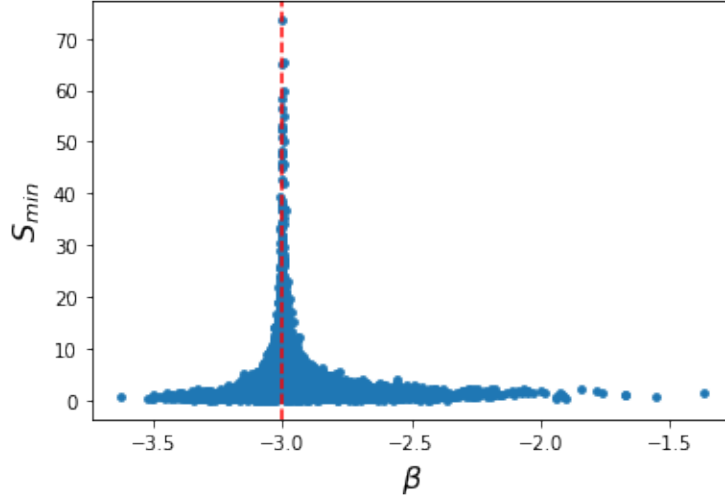


Figure 4.4: Scatter plot of the estimated β in each pixel against the minimum SNR among the four simulated P maps (S_{min}), in that pixel. Dashed line shows the true value $\hat{\beta} = -3$ used in simulations.

estimates of the true spectral index.

As an aside, we study the effect of using fewer input datasets on the estimated spectral index map. The red histogram in Figure 4.6 shows the distribution of recovered β values when a set of simulated P maps at all four survey frequencies are used, as done before. Next, we only used the P maps at the S-PASS (2.3 GHz) and WMAP K-band (22.8 GHz) frequencies. In this case, the combined likelihood is a product of the Rician factors (equation 3.12) for only these two frequencies. The corresponding posterior is maximized, and the resulting β values are distributed as shown by the blue line in Figure 4.6. The same procedure is repeated by pairing a simulated S-PASS P map with a map at the WMAP Ka-band frequency (33 GHz, green line), and alternatively with a map at the Planck-30 frequency (22.8 GHz, purple line). The histogram for (S-PASS+WMAP Ka-band) is broader than the other two since the SNR of the WMAP Ka-band map is lower than that of WMAP K-band and Planck-30 maps.

Since the red histogram is more sharply peaked around the true value as compared to the histograms obtained using fewer P maps, it is clear that using P maps at all four frequencies simultaneously results in more accurate estimates of β . This is because the SED of synchrotron emission is effectively constrained at four frequencies instead of just two. On the other hand, we verified that the estimates of β values obtained by omitting the S-PASS P map are extremely poor, since the synchrotron signal is order of 1000 times stronger for S-PASS, which has a much better

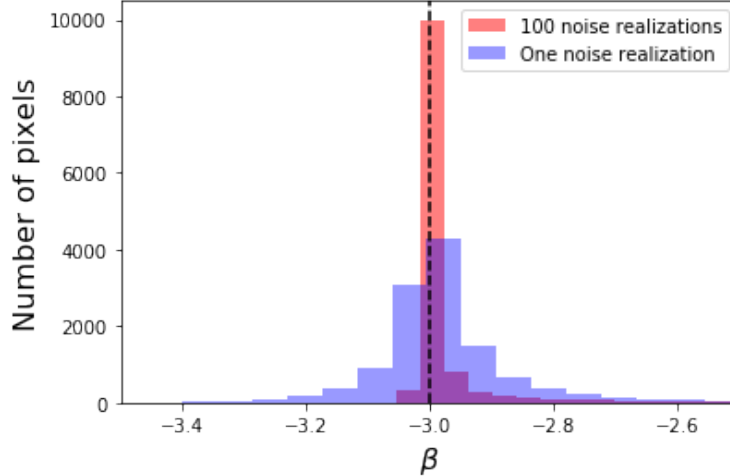


Figure 4.5: Histogram of the estimated β in each pixel, for simulated P maps with one set of noise realizations (blue), and histogram of averaged β with 100 sets of noise realizations (red). Dashed line shows the true value $\hat{\beta} = -3$ used in simulations. (Total number of pixels here is 12288, since we have considered full $N_{side} = 32$ maps. Number of bins = 40).

SNR. This is in agreement with previous analyses [31], [37] which have indicated the crucial role of radio datasets like S-PASS for investigating diffuse Galactic synchrotron emission.

Therefore, in the rest of our project, we use P maps at all the four survey frequencies together. Furthermore, we note that our methodology and likelihood can be adapted for simultaneously including more number of datasets as they become available (such as QUIJOTE and C-BASS South), which would likely yield more accurate estimates of the real spectral index map.

4.3 Estimating the spectral index using MCMC

In the previous section, we estimated the spectral index from simulated P maps by using a deterministic technique to optimize the posterior function. Now, we alternatively use the stochastic technique of Markov Chain Monte Carlo (MCMC) methods for the optimization process. The posterior function in equation 3.13 is the probability distribution of the two free parameters A_0 and β , given that the polarization P maps have been observed. MCMC allows us to numerically sample and investigate this posterior distribution.

Monte-Carlo is the approach of estimating a distribution by drawing random samples from

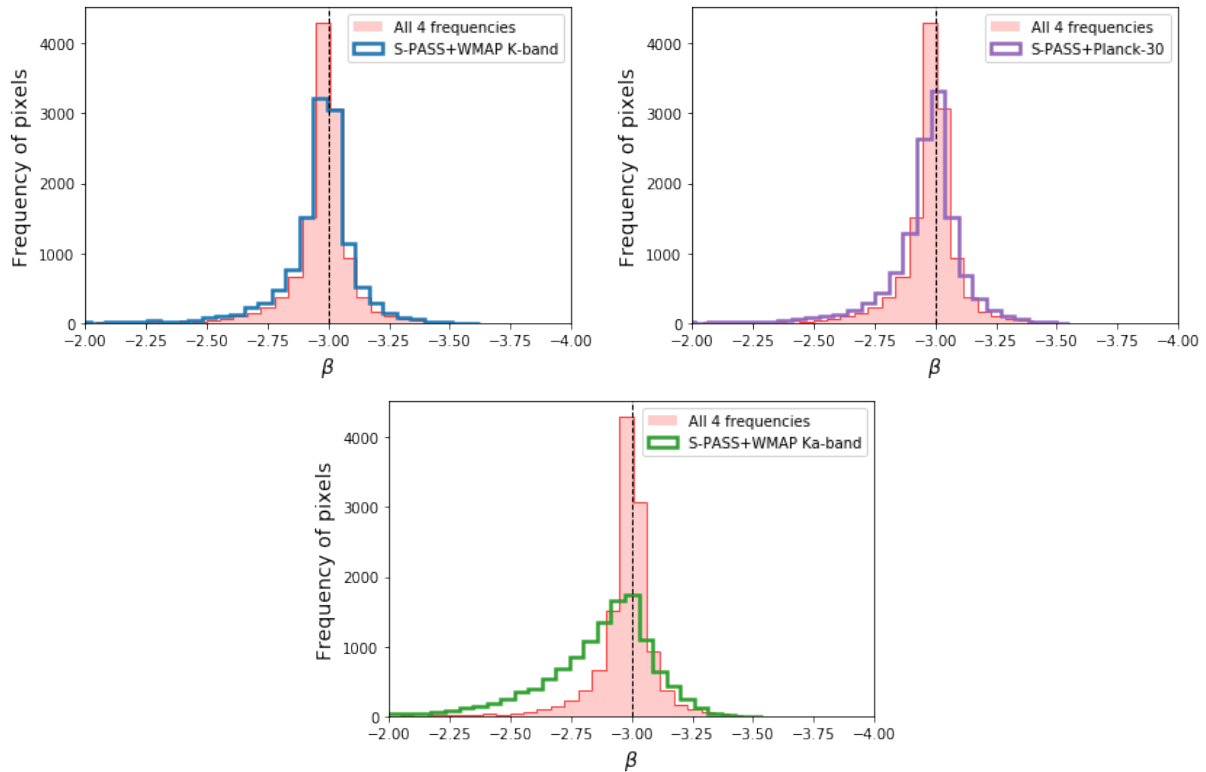


Figure 4.6: Comparing histograms of the estimated β values obtained using a set of simulated P maps at all 4 survey frequencies (red), with the values obtained using a simulated P map at the S-PASS frequency together with a P map at the WMAP K-band (blue line), WMAP Ka-band (green line), or Planck-30 (purple line) frequencies respectively. (Number of bins=40). Dashed line shows the true value $\hat{\beta} = -3$ used.

it. Markov-chain refers to the property of generating a new random sample solely based on the sample just preceding it. The Metropolis-Hastings algorithm for MCMC incorporates both these properties to generate a sequence of random samples that converge towards the given distribution. We implemented this algorithm in Python using PyMC.

We generate a chain of 350,000 samples in total, independently for each pixel. The first 150,000 steps among these are discarded as the burn-in period, during which the Markov chains converge sufficiently early. The remaining 200,000 steps are thinned further by only considering every tenth sample, to ensure that they are not correlated with each other. These parameter values were selected by studying the convergence of MCMC chains from our simulated P maps. Note that we restricted the analysis to the masked region which we used later for the real datasets, as explained in Chapter 3. It included the pixels covered by S-PASS which were at Galactic latitudes above 20° , comprising about 30% of the full sky.

In each pixel, the MCMC chain of β values samples the posterior distribution. We estimate the spectral index map and the error associated with it by calculating the mean and standard deviation of β values of the chains, respectively. The visualized maps are shown in Figure 4.7. As expected, the uncertainties on β are higher for pixels with low SNRs. Figure 4.8 shows the distribution of the estimated mean β values, which peaks at the true value of $\hat{\beta} = -3$ used in simulations. The average estimated spectral index across the map is -3.01 ± 0.11 , thus recovering largely unbiased estimates of the true value on an average.

4.3.1 Sampling the posterior

MCMC methods also enable us to investigate the shape and behaviour of our posterior distribution, in the 2-dimensional parameter space formed by A_0 and β . As suggested by our tests in the previous section, we specifically focus on one pixel with high SNRs (having the maximum S_{min}), and on another pixel with low SNRs (having the minimum S_{min}). Figure 4.9 shows the posterior distribution of the estimated parameters, as sampled by their corresponding MCMC chains.

The estimated mean β values for the high-SNR and low-SNR pixels are -2.98 and -3.15, respectively. Note that for the high-SNR pixel, the mean estimated β value matches the β value at which the posterior peaks, since its distribution is symmetric and well-behaved like a Gaussian. On the other hand, for the low-SNR pixel, equation 4.1 predicts that the likelihood is non-Gaussian,

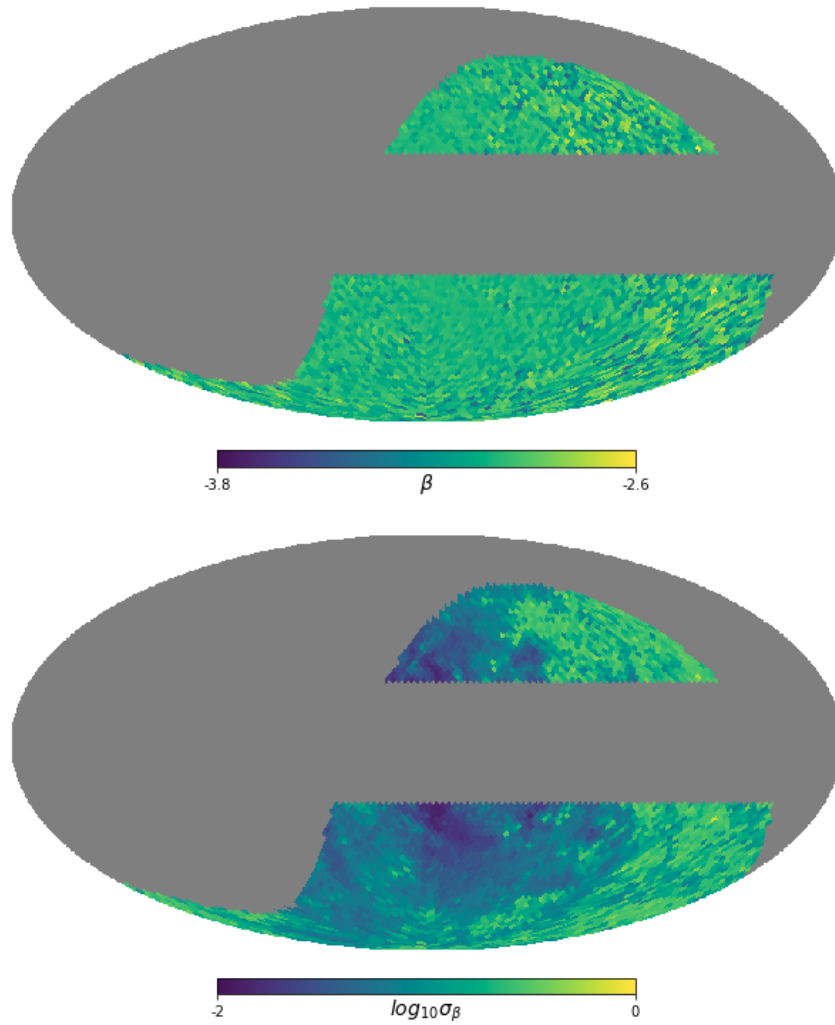


Figure 4.7: Maps of the mean (top) and standard deviation (bottom) of estimated β values of MCMC samples generated from simulated P maps. Colours are saturated for the purpose of visualization.

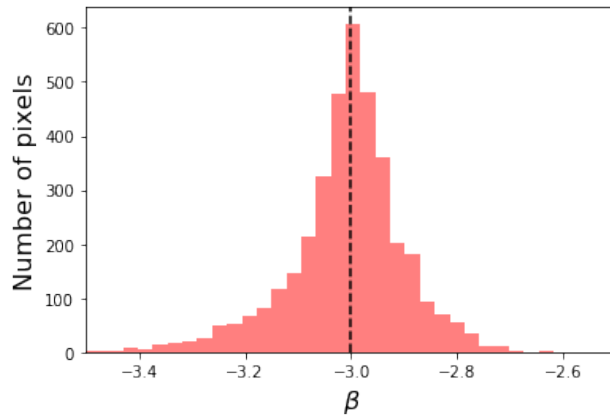


Figure 4.8: Histogram of the estimated mean β from MCMC chains in each pixel, for simulated P maps with a true value $\hat{\beta} = -3$ as shown by the dashed line. (Total number of pixels here is 3739).

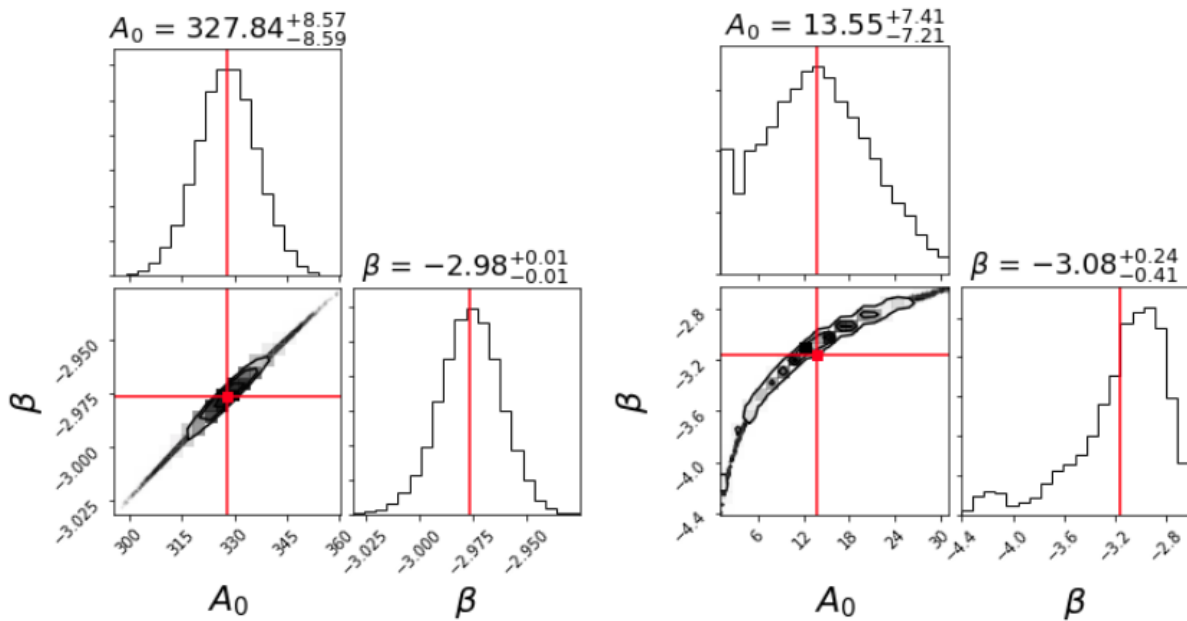


Figure 4.9: Corner plots for a pixel with high SNRs (left) and for a pixel with low SNRs (right), showing the respective posterior distributions of their two parameters. Red lines denote the set of parameter values at which the posterior peaks.

which leads to a skewed posterior with an unusual distribution, as shown in Figure 4.9. In this case, the mean β is different from the β value at which the posterior peaks, resulting in much higher uncertainties on the estimated spectral index for low-SNR pixels. Moreover, the peculiar shape of the posterior for low-SNR pixels may cause the Markov chains to converge without sampling the whole posterior, possibly inducing additional systematic errors on their β values. This analysis motivates us to further identify pixels which may have such uncertainties associated with them. We do this in the context of investigating the real diffuse Galactic synchrotron emission by using the actual datasets, as described in the next chapter.

Chapter 5

Results on Data

In this Chapter, we discuss results obtained from real datasets. In Section 5.1, we describe the actual spectral index β map, estimated by applying the methodology which we tested on simulations in the previous Chapter. In Section 5.2, we introduce a threshold to identify pixels for which the estimated β is considerably reliable. In the following Section, we quantify the variation in the β map by computing its angular power spectrum. Finally, in the Discussion, we compare our results with other related works, and discuss their possible implications in the context of CMB B-mode contamination.

5.1 Reconstructed spectral index map with errors

We first calculate polarization P maps at a resolution of $N_{side} = 32$, from the measured Q and U maps for each of our four datasets. We then combine these together using the method described earlier, in order to estimate the real spectral index map of diffuse Galactic synchrotron emission. Figure 5.1 shows the β map estimated by using the `scipy` optimizer to fit jointly for β and A_0 , by maximizing the posterior. Fluctuations in β are observed across the map, along with features like loops and spurs near the Galactic centre, which are typical of diffuse Galactic emission. The values of the spectral index vary in the range $-4.3 \leq \beta \leq -1.8$, with an average value of $\beta = -3.21$ and a standard deviation of 0.23 across different pixels.

We also use the MCMC technique described earlier to generate chains of random samples for

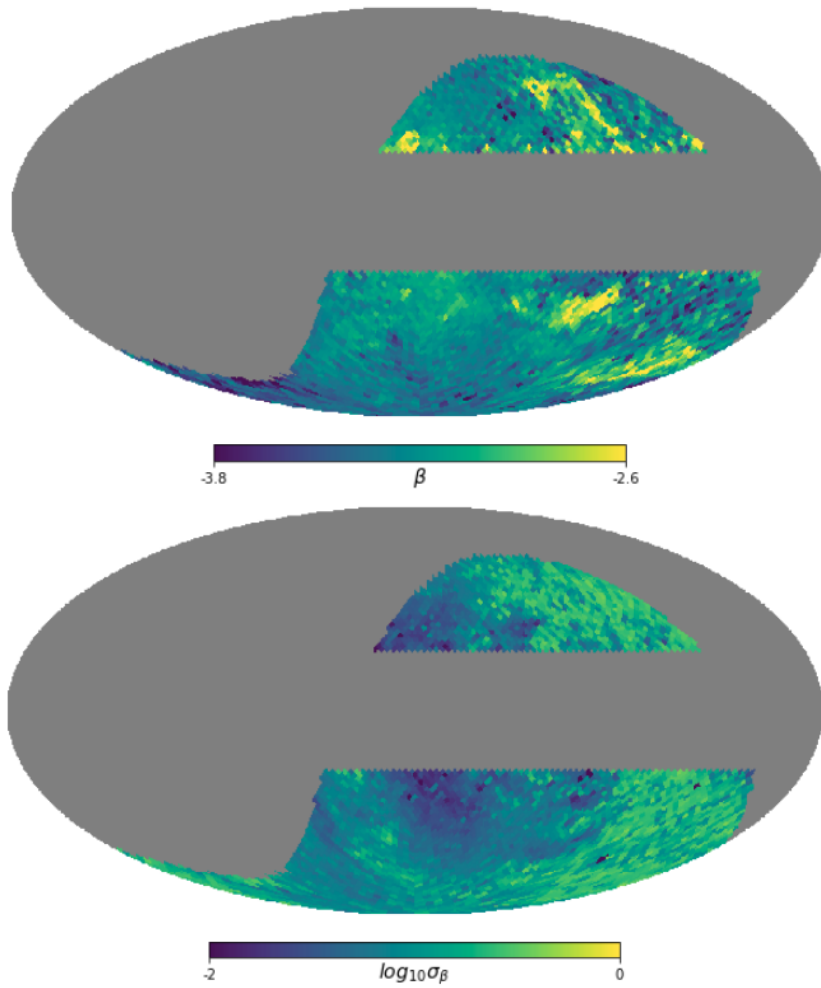


Figure 5.1: Synchrotron spectral index β map (top) and the 1σ uncertainty (bottom), estimated using P maps from real datasets. Colours are saturated for the purpose of visualization. Actual ranges of values are: $-4.3 \leq \beta \leq -1.8$ and $-3.6 \leq \log_{10}\sigma_{\beta} \leq -0.39$.

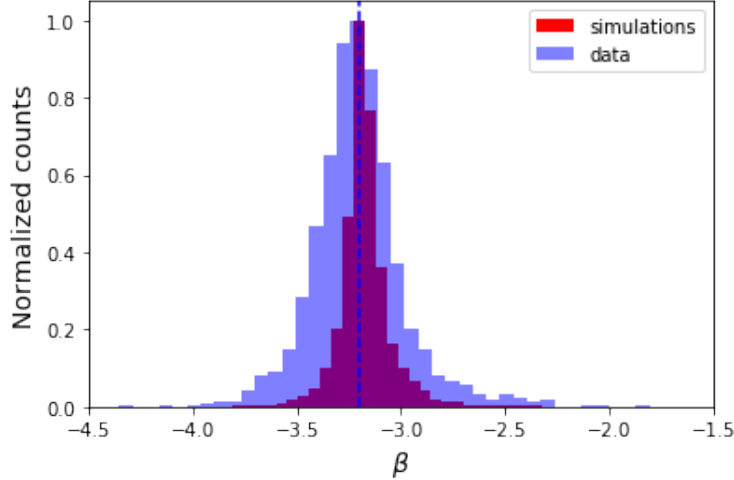


Figure 5.2: Comparing normalized histograms of the estimated spectral index in each pixel from data (blue), and from corresponding simulations (red). β peaks at about -3.2 for the estimates from data, as indicated by the dashed line.

each pixel. The average of the β values at the peak of the posterior for each chain is -3.26 , with a standard deviation of 0.29 across different pixels. This value is in agreement, but also differs slightly from the one above, probably due to partial sampling of the posterior for low SNR pixels. Following our tests on simulations, MCMC likely gives slightly biased estimates of β owing to the peculiar shape of our posterior distribution. Since the deterministic technique is quite robust, we choose the best-fit β map obtained from it for further analysis. The standard deviation of β in MCMC chains for each pixel provides an estimate of the error on our β map, as shown in the second map in Figure 5.1. As expected, statistical errors are smaller for pixels with higher SNR values in the data, which are closer to the Galactic plane or centre. The β value is recovered with an average 1σ error of 0.12 across all pixels, and with an uncertainty less than 0.1 for about 53% of the pixels.

Figure 5.2 shows the normalized histogram of the β values estimated in each pixel using data, which peaks at -3.2 . In order to investigate further the variation in β , we compare this distribution with the one obtained from simulations. We construct simulated P maps by extrapolating the nearly noiseless S-PASS P map (at $N_{side} = 32$) using a fixed spectral index of $\beta_{sim} = -3.2$ for all pixels. We add one noise realization to each of these signal maps, and estimate the β values using the same procedure. The histogram from simulations peaks at a value of -3.2 , with a symmetric distribution about it due to noise, confirming that our method yields unbiased estimates. In comparison, the data histogram has a wider spread, and is slightly asymmetric. This indicates that there is a real,

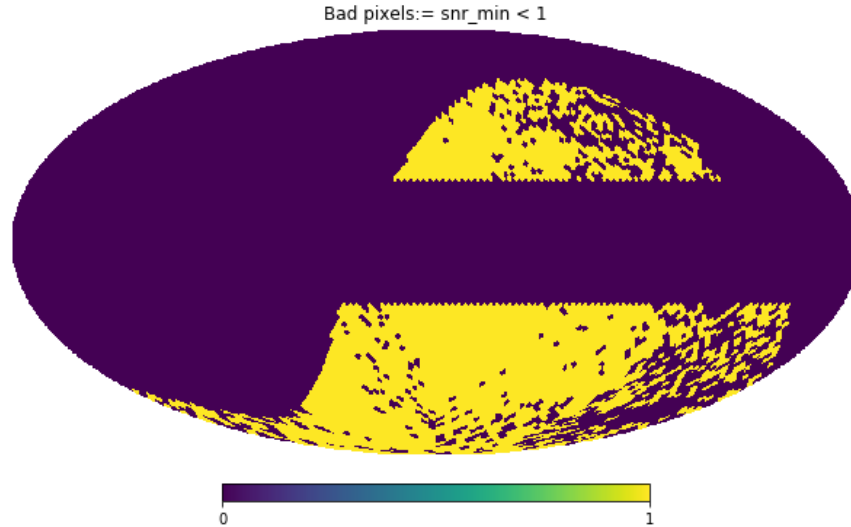


Figure 5.3: Mask showing pixels selected by the threshold, for which the obtained β is likely to be a reliable estimate of the true value.

physical spatial variation in β , in addition to the distribution caused by noise alone. This spatial complexity could arise from changes in the magnetic field strength, injected energy of cosmic rays, line-of-sight effects etc. across different regions of the sky.

5.2 Identifying reliable pixels

As above, we expect the true value of the synchrotron spectral index to vary across the sky. Since the presence of noise induces errors, it is useful to identify pixels for which the obtained β value is likely to be a reasonably accurate estimate of the true value. For each pixel, S_{min} is the minimum SNR value among the four datasets, as defined. We now introduce a threshold which rejects all pixels for which $S_{min} < 1$, i.e. for which the noise is larger than the P signal magnitude for some dataset. Around 75% pixels among the original region are retained, as shown in Figure 5.3. From our tests on simulations, we expect the estimated β values in the rejected pixels to be highly biased.

An advantage of generating sample chains with the MCMC technique is that it enables us to study the posterior distribution in detail. For each pixel, we fit jointly for A_0 and β ; we then evaluate the mean of β values of its MCMC chain, and also the β value at which the posterior peaks among the samples (or the *mode* value). The difference between the mean and mode value

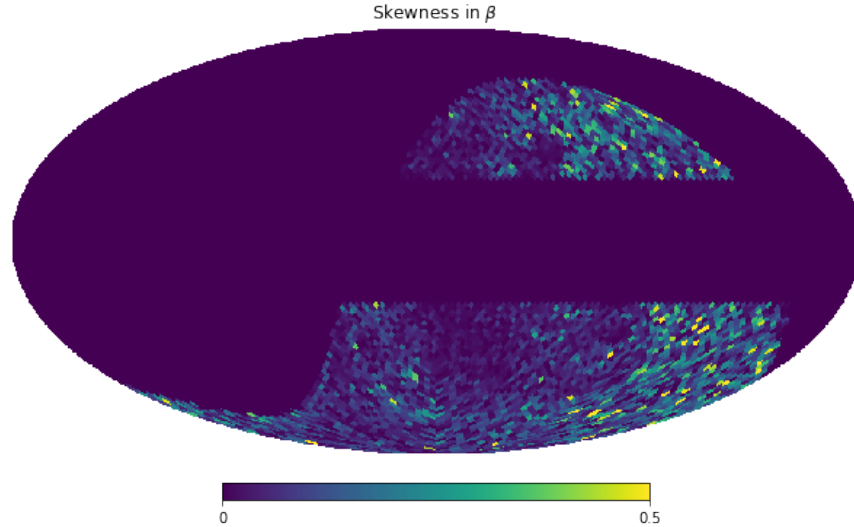


Figure 5.4: Map showing the absolute difference between the mean and mode of β values in MCMC chains for each pixel, used as a rough measure of the skewness of the posterior distribution.

of β is a rough measure of the skewness of the posterior in that pixel. From Figure 5.4, we see that most of the pixels with a significantly skewed posterior are removed by our above threshold. A *bad* pixel has $S_{min} < 1$ and low SNRs, which result in a skewed posterior with a peculiar distribution. As mentioned earlier, this can lead to a less accurate estimate of β even using the deterministic technique.

The average estimated β value among the pixels selected by our threshold is -3.19 , with a mean 1σ error of 0.09 across pixels, which agrees with the overall value of -3.21 ± 0.12 . The pixels selected by the threshold thus have smaller errors associated with them. Moreover, for the rejected pixels, the actual uncertainty on β would be higher than the standard deviation, since their posterior distributions are skewed and highly non-Gaussian. Across the selected pixels, the estimated β has a standard deviation of 0.19 , which indicates a smaller variation than the overall case.

As an aside, we note that the pixels rejected by our threshold were also mostly removed from their analysis by the S-PASS collaboration [44], while estimating the Faraday rotation in polarized S-PASS data. For the removed pixels, there was a large difference in the polarization angle maps of WMAP and Planck which was beyond Faraday rotation, possibly due to residual calibration errors in these maps [44]. While the polarization angle is not directly relevant for us here, it is possible that such residual errors could also lead to larger errors in P maps for these ‘bad’ pixels with low signal magnitudes.

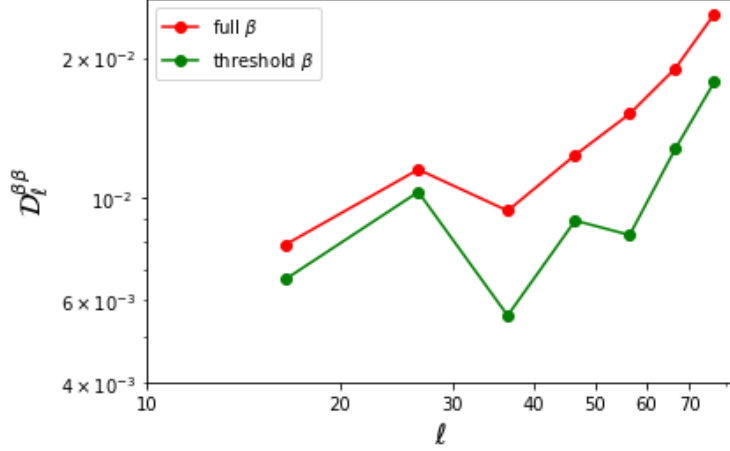


Figure 5.5: Angular power spectrum of the full spectral index β map (red), and angular power spectrum of the β map in the restricted masked region (Figure 5.3) given by our threshold (green). Both spectra have a partial contribution from spatial variations due to noise.

5.3 Angular power spectrum

In Section 1.5, we had introduced the concept of power spectrum as a statistical quantity to describe the distribution of anisotropies in the CMB. Now, we evaluate the angular power spectrum of our spectral index map, for the purpose of quantifying the amplitude of variations in β as a function of the angular scale l . Since our β map only covers a masked (30%) portion of the full sky, we use the python implementation of the code NaMaster¹ [50] in order to compute the 'pseudo- C_l ' for estimating the angular auto-power spectrum, $C_l^{\beta\beta}$.

Since our map is at an $N_{side} = 32$, the maximum permissible multipole is $l = 95$. We therefore compute $C_l^{\beta\beta}$ in the range $l = 10 - 80$, with a binsize of $\Delta l = 10$. It is shown in Figure 5.5 (red curve), where we have plotted the dimensionless quantity $D_l^{\beta\beta} \equiv C_l^{\beta\beta} l(l+1)/2\pi$. We repeat this procedure for the masked region shown in Figure 5.3, to evaluate the β power spectrum for only those pixels selected by the threshold described in the previous Section. In Figure 5.5, we note that the amplitude of variations in β in this restricted region is lower as compared to our whole β map. This is expected since the rejected pixels have very low SNRs, and highly biased estimates of β . The shape and slope of the power spectra are significantly different for the β map in the full and restricted regions.

¹See <https://github.com/LSSTDESC/NaMaster>

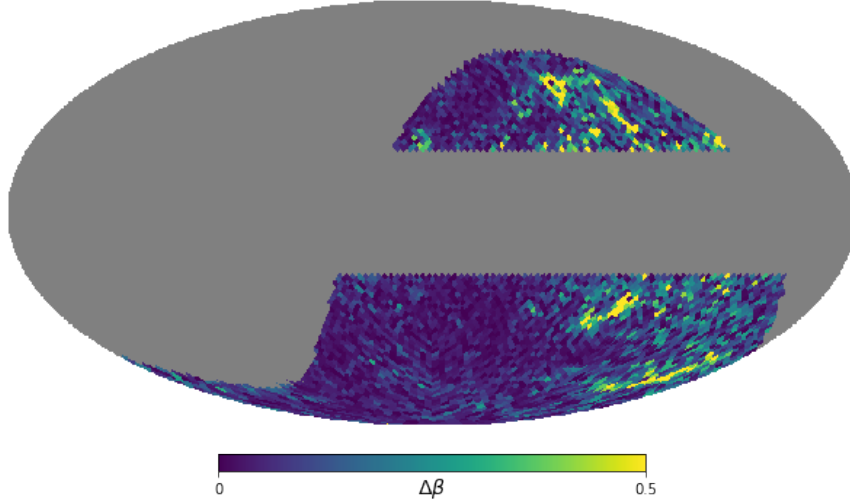


Figure 5.6: Absolute difference between our estimated spectral index map and the corresponding map [37] downgraded to an $N_{side} = 32$. Colours are saturated for visualization.

We found that the amplitude of the power spectrum for our full spectral index map is higher than the corresponding one reported [37]. We are currently investigating this deviation in more detail. As a later step, we will be quantifying and removing the noise bias from our power spectra, since the presence of noise in the WMAP and Planck datasets contributes partially towards the variations in the estimated β . We further discuss these results in the following Section.

5.4 Discussion

In this Section, we discuss our results from data in the context of previous works ([37]), and some of their implications for the contamination of the CMB B-mode due to diffuse Galactic synchrotron emission.

Recent work [37] combined the same datasets as ours, to study the Galactic synchrotron emission in the same sky region. They computed the auto- and cross-power spectra of the P maps, fit for their amplitude in harmonic space, and reported the mean β value as -3.22 ± 0.08 . They also empirically fitted for β in real space by comparing the data P maps with the extrapolated S-PASS polarization maps in the presence of noise. By considering 100 noise realizations, they estimated statistically the *first* β map using only polarization data, with a mean β value of -3.25 ± 0.15 . In contrast, we estimated our β map by mathematically considering the full effect of noise in an accu-

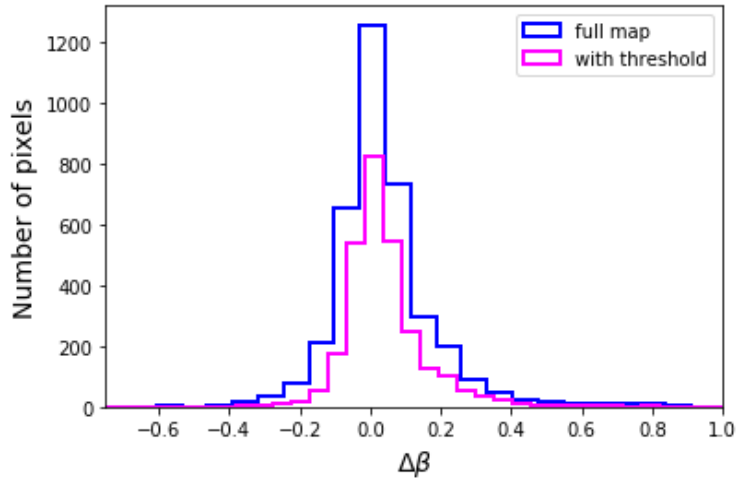


Figure 5.7: Histogram of the difference between our estimated spectral index and the corresponding value obtained [37], for each pixel in the full map (blue), and for each pixel in the masked region selected by our threshold (magenta).

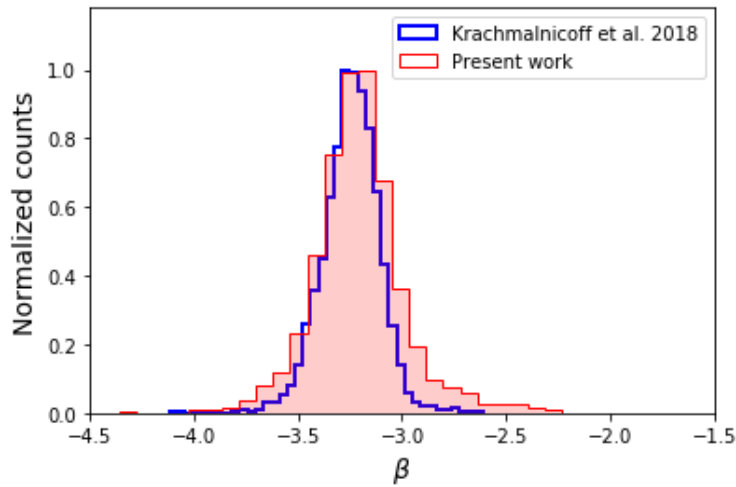


Figure 5.8: Comparing histograms of the estimated spectral index values for each pixel in our full β map (red), and in the β map [37] after downgrading it to an $N_{side} = 32$ (dark blue).

rate Bayesian framework. The mean β value of -3.21 ± 0.12 that we obtained is in agreement with their reported values, and with the value of -3.21 ± 0.15 reported by the S-PASS collaboration for $|b| > 30^\circ$ [44].

Figure 5.6 shows the absolute difference between our spectral index map and the one obtained [37] after downgrading it to $N_{side} = 32$. While the mean β values are consistent, we see a significant difference in the estimated β for some of the pixels. The root-mean-square deviation between the β values in the two spectral index maps is 0.16 for all the pixels, and 0.12 for the reliable pixels selected by our threshold. Figure 5.7 shows the distribution of the differences in the full and restricted cases. In both cases, the histogram is peaked at 0, indicating that the deviation is not skewed or biased systematically.

Therefore, the pixels with the largest differences are removed by our threshold due to prominent noise effects. Since the estimated β values of the selected pixels are reliable they constitute regions of the sky where the synchrotron emission is understood well. The synchrotron contamination in these regions could thus be estimated more accurately, making them more suitable for detecting the CMB B-mode, as compared to the rejected pixels.

Figure 5.8 shows that the spread in the distribution of β values in our spectral index map is higher. Therefore, the level of spatial variations in our spectral index map is significantly higher. This matches with our earlier result; the angular power spectrum of our β map has a much higher amplitude than the latter. In principle, the angular power spectrum can be extrapolated to other angular scales/multipoles. This can be used together with the estimated β map to generate simulations of the Galactic synchrotron polarization which would be more realistic than the existing PySM templates [36], thus providing a crucial tool for testing and developing component separation algorithms.

Previous analysis [37] used their mean spectral index to estimate the level of synchrotron contamination to the CMB B-mode in small sky regions, finding it to be equivalent to an r of order $10^{-2} - 10^{-3}$. They also used the mean β to evaluate the power spectrum of the B-mode polarization of diffuse Galactic synchrotron emission across different sky regions, as shown in Figure 2.2. Therefore, extensions and applications of our present work could potentially deepen our understanding of the spatially varying levels of contamination due to synchrotron emission, and provide insights for component separation of CMB foregrounds.

Chapter 6

Conclusions and Outlook

The CMB is the oldest electromagnetic radiation in the Universe, and a key cosmological probe. While most of the CMB temperature and E-mode polarization anisotropies have been accurately measured, most recently by Planck, detecting the CMB B-mode polarization is an active open problem. The CMB B-mode signal would provide direct evidence for primordial gravitational waves and the theory of inflation. This primordial signal is extremely faint, and is dominated by diffuse Galactic foreground emissions that contaminate the CMB observations. Characterization and removal of polarized foregrounds is a crucial observational challenge today. In this project, we have investigated the diffuse Galactic synchrotron emission as a contaminant in CMB B-mode observations.

Although thermal dust emission from our Galaxy is the major contaminant at higher frequencies, synchrotron emission is the dominant polarized foreground at frequencies below 70-100 GHz. Since the SED of synchrotron polarization theoretically falls as a power law in frequency, we have used the S-PASS dataset with a high SNR at 2.3 GHz, along with low frequency WMAP (23, 33 GHz) and Planck (28.4 GHz) datasets. We have followed a Bayesian framework for studying the frequency dependence of polarized synchrotron. The total polarization P is modelled as a Rician random variable, due to the presence of noise in the measured maps. In each pixel, we jointly fit for parameter values of the spectral index β and the SED amplitude, by maximizing the corresponding posterior.

We have validated this method by testing it on a set of simulated polarization maps. We find that the recovered estimates of β are unbiased in general, and are closer to the true value for pixels

with high SNRs in the P maps. We also find that for very low SNR pixels, the posterior has a peculiar distribution in the parameter space. Therefore, we preferentially use a robust deterministic technique to optimize the posterior and to estimate the β values, while using the MCMC method for estimating errors on β through random sampling. We further showed that using fewer datasets in the same framework gives less accurate estimates of β . This motivates the inclusion of additional datasets such as C-BASS and QUIJOTE in the northern hemisphere using our methodology, in order to obtain improved estimates of the diffuse Galactic synchrotron emission in the future.

We have applied the above methodology to our real data maps, and estimated a polarized synchrotron spectral index map with errors, for the considered sky region. We find a mean value of $\beta = -3.21 \pm 0.12$, which is in agreement with the previous empirical analysis [37]. We showed that the variation observed across our β map is a real feature, and not just arising due to noise. We have introduced a threshold that rejects pixels with a minimum SNR smaller than one, and shown that the β estimates for the remaining 75% pixels are expected to be reliable. Comparing our spectral index map with [37], we see that they differ sharply for some pixels, with an overall root-mean-square deviation of 0.16 across all pixels. Since our treatment of noise in the datasets is mathematically accurate and complete, we expect some differences with the results from other approaches.

We have also computed the angular power spectrum of our β map to quantify the spatial variation in β as a function of the angular scale. We also computed the spectrum for the restricted region selected by our threshold. The shape and slope of the power spectra are different with and without the threshold. Also, we noted that the amplitude of our full power spectrum is higher than [37], confirming further that our map has more spatial variation in β . We are currently investigating this deviation in detail. The power spectrum and our estimated β map can be used to build more realistic simulations, which are crucial for testing component separation algorithms.

In the future, we could possibly extend this work by estimating the amount of synchrotron contamination in CMB observations, in terms of its equivalent tensor-to-scalar ratio r_{synch} . This can be done by extrapolating the synchrotron signal to higher frequencies using a constant mean spectral index value across all pixels [37], or by using our spatially-varying estimated β map. A comparison of the resulting average r_{synch} values would indicate how much the spatial variation of synchrotron emission impacts its level of contamination. In addition, we could also use our spectral index map as a template, to forecast how the spatial variation of synchrotron affects component separation at different angular scales [51]. Our present work and its possible extensions

could therefore be very relevant for upcoming missions such as CMB-S4, Simons Observatory, and LiteBIRD, which aim to detect the inflationary CMB B-mode signal at large angular scales, and with low uncertainties on r .

Bibliography

- [1] Edwin Hubble. A relation between distance and radial velocity among extra-galactic nebulae. *Proceedings of the National Academy of Sciences*, 15(3):168–173, 1929.
- [2] Scott Dodelson. *Modern Cosmology*. Academic Press, Amsterdam, 2003.
- [3] Alan H. Guth. Inflationary universe: A possible solution to the horizon and flatness problems. *Phys. Rev. D*, 23:347–356, Jan 1981.
- [4] Andrei D. Linde. A New Inflationary Universe Scenario: A Possible Solution of the Horizon, Flatness, Homogeneity, Isotropy and Primordial Monopole Problems. *Phys. Lett.*, 108B:389–393, 1982. [Adv. Ser. Astrophys. Cosmol.3,149(1987)].
- [5] Edward W. Kolb and Michael S. Turner. *The Early Universe*, volume 69. 1990.
- [6] Scott Burles, Kenneth M. Nollett, and Michael S. Turner. Big bang nucleosynthesis predictions for precision cosmology. *The Astrophysical Journal*, 552(1):L1–L5, may 2001.
- [7] Wayne Hu and Martin White. A cmb polarization primer. *New Astronomy*, 2(4):323–344, Oct 1997.
- [8] Y. Akrami et al. Planck 2018 results. I. Overview and the cosmological legacy of Planck. 2018.
- [9] J. C. Mather, E. S. Cheng, Jr. Eplee, R. E., R. B. Isaacman, S. S. Meyer, R. A. Shafer, R. Weiss, E. L. Wright, C. L. Bennett, N. W. Boggess, E. Dwek, S. Gulkis, M. G. Hauser, M. Janssen, T. Kelsall, P. M. Lubin, Jr. Moseley, S. H., T. L. Murdock, R. F. Silverberg, G. F. Smoot, and D. T. Wilkinson. A Preliminary Measurement of the Cosmic Microwave Background Spectrum by the Cosmic Background Explorer (COBE) Satellite. .
- [10] R. Adam, P. A. R. Ade, N. Aghanim, Y. Akrami, M. I. R. Alves, F. Argüeso, M. Arnaud, F. Arroja, M. Ashdown, and et al. Planck2015 results. *Astronomy Astrophysics*, 594:A1, Sep 2016.
- [11] Matias Zaldarriaga and Uroš Seljak. All-sky analysis of polarization in the microwave background. *Physical Review D*, 55(4):1830–1840, Feb 1997.

- [12] Daniel Baumann, Mark G. Jackson, Peter Adshead, Alexandre Amblard, Amjad Ashoorioon, Nicola Bartolo, Rachel Bean, Maria Beltran, Francesco de Bernardis, Simeon Bird, and et al. Probing inflation with cmb polarization. *AIP Conference Proceedings*, 2009.
- [13] Uros Seljak and Matias Zaldarriaga. Signature of gravity waves in polarization of the microwave background. *Phys. Rev. Lett.*, 78:2054–2057, 1997.
- [14] Antony Lewis and Anthony Challinor. Camb: Code for anisotropies in the microwave background.
- [15] Joseph Silk. Cosmic Black-Body Radiation and Galaxy Formation. , 151:459, February 1968.
- [16] A. A. Penzias and R. W. Wilson. A Measurement of Excess Antenna Temperature at 4080 Mc/s. , 142:419–421, July 1965.
- [17] D. N. Spergel, L. Verde, H. V. Peiris, E. Komatsu, M. R. Nolta, C. L. Bennett, M. Halpern, G. Hinshaw, N. Jarosik, A. Kogut, and et al. First-year wilkinson microwave anisotropy probe (wmap) observations: Determination of cosmological parameters. *The Astrophysical Journal Supplement Series*, 148(1):175–194, Sep 2003.
- [18] National Aeronautics and Space Administration (NASA). Data hosted on lambda: Cmb experiments.
- [19] N. Aghanim et al. Planck 2018 results. VI. Cosmological parameters. 2018.
- [20] The Polarbear Collaboration: P. A. R. Ade, Y. Akiba, A. E. Anthony, K. Arnold, M. Atlas, D. Barron, D. Boettger, J. Borrill, S. Chapman, Y. Chinone, and et al. A measurement of the cosmic microwave backgroundb-mode polarization power spectrum at sub-degree scales with polarbear. *The Astrophysical Journal*, 794(2):171, Oct 2014.
- [21] Detection of *b*-mode polarization at degree angular scales by bicep2. *Phys. Rev. Lett.*, 112:241101, Jun 2014.
- [22] P. A. R. Ade et al. Joint Analysis of BICEP2/KeckArray and *Planck* Data. *Phys. Rev. Lett.*, 114:101301, 2015.
- [23] Raphael Flauger, J. Colin Hill, and David N. Spergel. Toward an understanding of foreground emission in the bicep2 region. *Journal of Cosmology and Astroparticle Physics*, 2014(08):039–039, Aug 2014.
- [24] The Polarbear-2 and the Simons Array Experiments. *Journal of Low Temperature Physics*, 184(3-4):805–810, August 2016.
- [25] R. J. Thornton, P. A. R. Ade, S. Aiola, F. E. Angilè, M. Amiri, J. A. Beall, D. T. Becker, H-M. Cho, S. K. Choi, P. Corlies, and et al. The atacama cosmology telescope: The polarization-sensitive actpol instrument. *The Astrophysical Journal Supplement Series*, 227(2):21, Dec 2016.

- [26] SPTpol: an instrument for CMB polarization measurements with the South Pole Telescope. In Wayne S. Holland, editor, *Millimeter, Submillimeter, and Far-Infrared Detectors and Instrumentation for Astronomy VI*, volume 8452, pages 393 – 410. International Society for Optics and Photonics, SPIE, 2012.
- [27] Improved constraints on cosmology and foregrounds from bicep2 and keck array cosmic microwave background data with inclusion of 95 ghz band. *Phys. Rev. Lett.*, 116:031302, Jan 2016.
- [28] Peter Ade, James Aguirre, Zeeshan Ahmed, Simone Aiola, Aamir Ali, David Alonso, Marcelo A. Alvarez, Kam Arnold, Peter Ashton, Jason Austermann, and et al. The simons observatory: science goals and forecasts. *Journal of Cosmology and Astroparticle Physics*, 2019(02):056–056, Feb 2019.
- [29] Kevork N. Abazajian et al. CMB-S4 Science Book, First Edition. 2016.
- [30] *LiteBIRD: a small satellite for the study of B-mode polarization and inflation from cosmic background radiation detection*, volume 8442 of *Society of Photo-Optical Instrumentation Engineers (SPIE) Conference Series*, page 844219. 2012.
- [31] N. Krachmalnicoff, C. Baccigalupi, J. Aumont, M. Bersanelli, and A. Mennella. Characterization of foreground emission on degree angular scales for CMB B-mode observations - Thermal dust and synchrotron signal from Planck and WMAP data. *Astron. Astrophys.*, 588:A65, 2016.
- [32] A. Kogut, J. Dunkley, C. L. Bennett, O. Dore, B. Gold, M. Halpern, G. Hinshaw, N. Jarosik, E. Komatsu, M. R. Nolta, N. Odegard, L. Page, D. N. Spergel, G. S. Tucker, J. L. Weiland, E. Wollack, and E. L. Wright. Three-Year Wilkinson microwave anisotropy probe(WMAP) observations: Foreground polarization. *The Astrophysical Journal*, 665(1):355–362, aug 2007.
- [33] Ransom S. M. Condon J. J. J. J. *Essential radio astronomy*, p. 361. 2016.
- [34] A.E. Vladimirov, S.W. Digel, G. Jóhannesson, P.F. Michelson, I.V. Moskalenko, P.L. Nolan, E. Orlando, T.A. Porter, and A.W. Strong. Galprop webrun: An internet-based service for calculating galactic cosmic ray propagation and associated photon emissions. *Computer Physics Communications*, 182(5):1156–1161, May 2011.
- [35] George B. Rybicki and Alan P. Lightman. *Radiative processes in astrophysics*. 1979.
- [36] B. Thorne, J. Dunkley, D. Alonso, and S. Næss. The python sky model: software for simulating the galactic microwave sky. *Monthly Notices of the Royal Astronomical Society*, 469(3):2821–2833, May 2017.

- [37] N. Krachmalnicoff, E. Carretti, C. Baccigalupi, G. Bernardi, S. Brown, B. M. Gaensler, M. Haverkorn, M. Kesteven, F. Perrotta, S. Poppi, and et al. S-pass view of polarized galactic synchrotron at 2.3 ghz as a contaminant to cmb observations. *Astronomy Astrophysics*, 618:A166, Oct 2018.
- [38] Draine B. T. *Physics of the interstellar and intergalactic medium*, p. 540. Princeton University Press, 2011.
- [39] R. Adam, P. A. R. Ade, N. Aghanim, M. I. R. Alves, M. Arnaud, M. Ashdown, J. Aumont, C. Baccigalupi, A. J. Banday, and et al. Planck 2015 x. diffuse component separation: Foreground maps. *Astronomy Astrophysics*, 594:A10, Sep 2016.
- [40] N. Macellari, E. Pierpaoli, C. Dickinson, and J. E. Vaillancourt. Galactic foreground contributions to the 5-year Wilkinson Microwave Anisotropy Probe maps. *Monthly Notices of the Royal Astronomical Society*, 418(2):888–905, 2011.
- [41] B. T. Draine and A. Lazarian. Electric dipole radiation from spinning dust grains. *The Astrophysical Journal*, 508(1):157–179, Nov 1998.
- [42] Quijote scientific results – i. measurements of the intensity and polarisation of the anomalous microwave emission in the perseus molecular complex. *Monthly Notices of the Royal Astronomical Society*, 452(4):4169–4182, Aug 2015.
- [43] Radek Stompor, Josquin Errard, and Davide Poletti. Forecasting performance of cmb experiments in the presence of complex foreground contaminations. *Physical Review D*, 94(8), Oct 2016.
- [44] E Carretti, M Haverkorn, L Staveley-Smith, G Bernardi, B M Gaensler, M J Kesteven, S Poppi, S Brown, R M Crocker, C Purcell, and et al. S-band polarization all-sky survey (s-pass): survey description and maps. *Monthly Notices of the Royal Astronomical Society*, 489(2):2330–2354, Sep 2019.
- [45] Michael E Jones, Angela C Taylor, Moumita Aich, C J Copley, H Cynthia Chiang, R J Davis, C Dickinson, R D P Grumitt, Yaser Hafez, Heiko M Heilgendorff, and et al. The c-band all-sky survey (c-bass): design and capabilities. *Monthly Notices of the Royal Astronomical Society*, 480(3):3224–3242, Jul 2018.
- [46] Christopher Sheehy and Anže Slosar. No evidence for dust b-mode decorrelation in planck data. *Physical Review D*, 97(4), Feb 2018.
- [47] Planck intermediate results - l. evidence of spatial variation of the polarized thermal dust spectral energy distribution and implications for cmb b-mode analysis. *A&A*, 599:A51, 2017.
- [48] U. Fuskeland, K. J. Andersen, R. Aurlien, R. Banerji, M. Brilenkov, H. K. Eriksen, M. Galloway, E. Gjerløw, S. K. Næss, T. S. Svalheim, and I. K. Wehus. Constraints on the spectral index of polarized synchrotron emission from wmap and faraday-corrected s-pass data, 2019.

- [49] K. M. Górski, E. Hivon, A. J. Banday, B. D. Wandelt, F. K. Hansen, M. Reinecke, and M. Bartelmann. HEALPix: A Framework for High-Resolution Discretization and Fast Analysis of Data Distributed on the Sphere. , 622:759–771, April 2005.
- [50] David Alonso, Javier Sanchez, and Anže Slosar. A unified pseudo-c framework. *Monthly Notices of the Royal Astronomical Society*, 484(3):4127–4151, Jan 2019.
- [51] Radek Stompor, Josquin Errard, and Davide Poletti. Forecasting performance of cmb experiments in the presence of complex foreground contaminations. *Phys. Rev. D*, 94:083526, Oct 2016.